

DRAFT v0.1 (4 AUGUST 2024)

Introduction to Dark Matter and Dark Sector Models and Searches

Yi-Ming Zhong^a

^a City University of Hong Kong, 83 Tat Chee Avenue, Kowloon, Hong Kong SAR, China

E-mail: yiming.zhong@cityu.edu.hk

ABSTRACT: Lecture notes for the 28th International Summer Institute on Phenomenology of Elementary Particle Physics and Cosmology (SI2024) at Linyi, Shangdong, China.

Contents

1	Introduction	1
2	First lecture	2
2.1	Evidence for dark matter	2
2.2	Basic properties of dark matter	2
2.3	Dark matter with dark sector mediators	6
2.4	Complementarity of different probes	7
2.5	The wall: N_{eff} constraints	12
3	Second lecture	18
3.1	Small-scale power spectrum: probing dark matter in the early universe	19
3.1.1	The power spectrum of CDM	20
3.1.2	The power spectrum of dark matter beyond CDM	22
3.1.3	Observations	26
3.2	Inside dark matter halos: self-interacting dark matter	26
A	Units	31
B	Cosmology for people in a hurry	31
B.1	Background	31
B.2	Thermodynamics in the early universe	31
B.3	Dark matter thermal freeze-out	33

1 Introduction

Two statements summarize our understanding of dark matter today: (1) dark matter exists, and (2) its nature remains elusive. There is a wealth of textbooks, reviews, community reports, lecture notes and video records on the subject of dark matter. Notable recent contributions include the review by [1], the text books by [2, 3], the TASI lectures by [4, 5], and video records by [6], which I heavily relied on in making this lecture notes. Given the vast scope of dark matter modeling and detection, it is impossible to cover all aspects comprehensively in these lectures. Therefore, I will focus on an emerging paradigm that I have been working on, where dark matter is considered part of the dark sectors. In this framework, additional particles in the dark sector serve as mediators for interactions between dark matter and ordinary matter, and for interactions among dark matter particles themselves. In Lecture I, I will provide a brief overview of dark matter and explore the complementarity of various probes from the intensity frontier experiment, while Lecture II will focus on the observational signatures at the small-scale structures.

Before concluding, I would like to share my favorite quote:

“It is difficult but interesting to master ten percent of any field. The path from ten to ninety percent is pure pleasure and genuine creativity. To go through the next nine percent is infinitely difficult, and far from everyone’s ability. The last percent is hopeless.”

— Yakov Zel’dovich

2 First lecture

2.1 Evidence for dark matter

Over the past 91 years, since Zwicky first proposed dark matter to explain the unexpected concentration of galaxies in the Coma cluster [7], evidence supporting its existence has accumulated across multiple cosmic scales. Dark matter has become an indispensable ingredient of the standard cosmology model, Λ CDM, where Λ represents for the cosmological constant while CDM stands for the “cold dark matter.” Dark matter has successfully explained various astronomical and cosmological observations, including: the behavior of galaxy clusters, galaxy rotation curves, bullet cluster crossing, the formation of large-scale structure (LSS), cosmic shear, and the patterns in the cosmic microwave background (CMB), see e.g. [8, 9] for a review. Fig. 2 presents a timeline of significant events in the development of dark matter physics. In this timeline, events highlighted in color represent major observational evidence supporting the existence of dark matter. Events shown in black text indicate important proposed dark matter candidates, related phenomena, or key methodologies used in dark matter research.

2.2 Basic properties of dark matter

Yet the nature of dark matter remains elusive. This does not mean we do not know any properties of dark matter. In fact, we have a good understanding of dark matter’s behavior on large scales. To agree with observations from the CMB, Big Bang nucleosynthesis (BBN), and LSS, dark matter must be:

- Cold: dark matter is non-relativistic ($v \ll c$) during the gravitational collapse.
- Non-baryonic
- Stable
- The abundance of dark matter today is $\Omega_\chi h^2 = 0.1200 \pm 0.001$ where $h = 0.674 \pm 0.005$ is the reduced Hubble constant from Planck 2018 [10]. The abundance corresponds to a background dark matter density of $\rho_\chi = 1.3 \text{ keV cm}^{-3} \simeq 10^{-11} \text{ eV}^4$.¹

Dark matter is about five times greater than that of the baryonic matter. While this factor of five may seem large, it is relatively small compared to the ratio of dark matter abundance to the photon abundance today ($\Omega_\gamma h^2 = 2 \times 10^{-5}$), which is about 5,000 times. The closeness in the abundance between dark matter and baryons lead to the idea of asymmetric dark matter.

¹Here and below, we use the natural unit $\hbar = c = k_B = 1$. See Appendix A for more details.

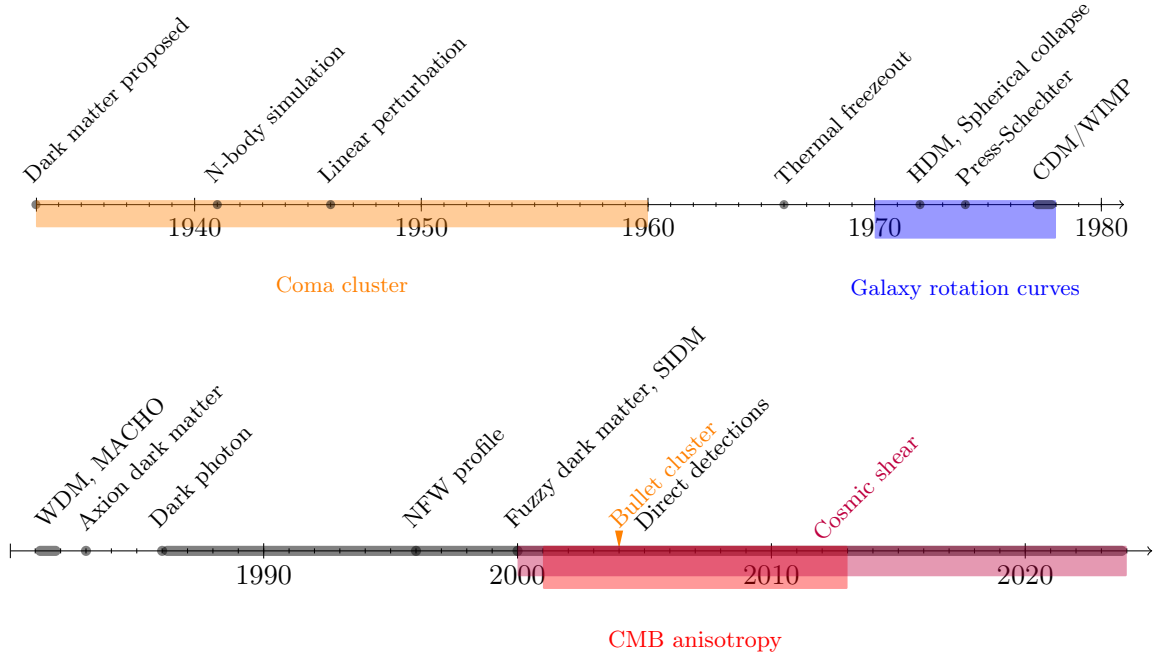


Figure 1. A brief history of dark matter and related theories and methodologies. Source: [1, 8, 9]. Acronym: CDM: cold dark matter; HDM: hot dark matter; WDM: warm dark matter; SIDM: self-interacting dark matter; WIMP: weakly-interacting massive particle; MACHO: massive compact halo object.

- Adiabatic: dark matter has the same primordial density fluctuations as baryons, photons, and neutrinos on the cosmic scale. The constraint from CMB anisotropy on the departure from the adiabatic fluctuations is about $\mathcal{O}(10^{-2})$.

The adiabatic property is usually used to constrain multi-field inflation models, some recent attempts tried to use the properties to constrain dark matter production via freeze-in [11] and later studies found the observational constraints are actually not strong at all [12–15].

Small-scale observations also provide values on dark matter local density and constrain dark matter’s “particle” mass, whether as an individual particle or a single composite object:

- The local dark matter density is $\rho_\chi = 0.4 \text{ GeV cm}^{-3} \simeq (0.04 \text{ eV})^4$ [16].
- Dark matter cannot be too light, $m \gtrsim 10^{-22} \text{ eV}$, as its de Broglie wavelength would then exceed the virial radius of a dwarf galaxy. Otherwise, the bulk of the dwarf halo will reside in a soliton region, which has a ultra-higher density that is in tension with observations [17].
- Dark matter cannot be too heavy, $m \lesssim 10^4 M_\odot$, as there should be a sufficient number of particles to populate a dwarf galaxy such that its density distribution and gravitational field are mostly smooth and do not show granularity.

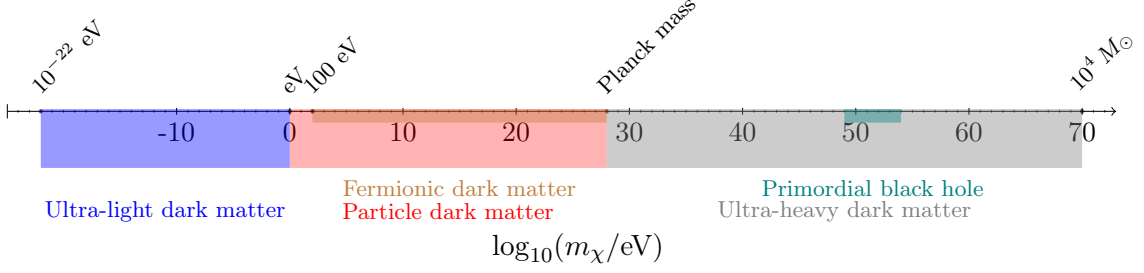


Figure 2. Important mass scales for dark matter candidates between 10^{-22} eV and $10^4 M_\odot$. We split them into ultra-light dark matter ($\lesssim 1$ eV), particle dark matter ($1 \text{ eV} - m_{\text{pl}}$), ultra-heavy dark matter ($\gtrsim m_{\text{pl}}$). We also show the mass range for fermionic particle dark matter and the primordial black hole as the dominant component of dark matter.

The mass of dark matter “particles” spans over 90 orders of magnitude ($1 M_\odot \simeq 10^{66} \text{ eV} \simeq 2 \times 10^{33} \text{ g}$). Yet it is still finite. There are a few important mass scales on the vast range of dark matter mass:

- $m_\chi = m_{\text{pl}} \simeq 10^{28} \text{ eV} \simeq 22 \mu\text{g}$, above which a single dark matter particle’s Compton wavelength will be within its Schwarzschild radius

$$m_\chi \gtrsim m_{\text{pl}} \quad \Rightarrow \quad \frac{1}{m_\chi} \lesssim G m_\chi = \frac{m_\chi}{m_{\text{pl}}^2}. \quad (2.1)$$

Therefore for dark matter “particle” with $m_\chi > m_{\text{pl}}$, what we mean by “particle” is not a single particle, but a single composite object such as primordial black holes, or a bag of dark matter particles. I call those candidates as ultra-heavy dark matter.

- $m_\chi = 100 \text{ eV}$. If dark matter is fermionic, a halo can be considered as a self-gravitating degenerate Fermi gas system. For such a halo to exist, the Fermi velocity v_F , which is given by

$$v_F = \left(\frac{6\pi^2 \rho_\chi}{g_\chi m_\chi^4} \right)^{1/3} \quad (2.2)$$

with g_χ is the number of spin and flavor states, should not exceed the escape velocity of the halo. Assuming a halo has a uniform density, the condition yields

$$v_F \leq \sqrt{\frac{2GM_h}{r_h}} \Rightarrow m_\chi \gtrsim g_\chi^{-1/4} G^{-3/8} M_h^{-1/8} r_h^{-3/8}, \quad (2.3)$$

where M_h and r_h are the halo mass and radius, respectively. From the inequality, it is easy to see a stronger constraints can be obtained from a smaller halo. Ref. [18] analysis Leo II, a dwarf galaxy, and imposes a constraints of $m_\chi \geq 0.13 \text{ keV}$ for fermionic dark matter with $g = 2$.

- $m_\chi = 1 \text{ eV}$, below which particles’ de Broglie wavelength overlap with each other.

$$\frac{1}{m_\chi v_\chi} \geq \left(\frac{\rho_\chi}{m_\chi} \right)^{-1/3} \Rightarrow m_\chi \leq \rho_\chi^{-1/4} v_\chi^{-3/4} \sim \mathcal{O}(\text{eV}). \quad (2.4)$$

	Neutrinos	Dark Matter
Number of species	Three flavors	?
Mass	$0 - 0.8$ eV	$10^{-22} - 10^{70}$ eV
(Sum of masses)	$0.059 - 0.113$ eV	??
Spin	$1/2$?
Electric charge	0	$\lesssim 10^{-10} - 10^{-1}$
Self-interaction	Electroweak & ?	Gravity & ?
Int. w/ other particles	Electroweak & ?	Gravity & ?
Lifetime	$\gtrsim 6 \times 10^{15}$ s	$\gtrsim 4.4 \times 10^{17}$ s
Decay channel	?	?
Cosmic production	Decoupled from SM plasma at $T \sim 1$ MeV	?
Other prod. channel	Stars, cosmic rays, reactors, accelerators ...	?
Abundance today	$(1.4 - 2.7) \times 10^{-3}$	0.264
% of the total mass	$(0.4 - 0.9)\%$	84%
ρ_{bkg}	$(6.7 - 13)$ eV cm $^{-3}$	1.3 keV cm $^{-3}$
n_{bkg}	3×112 cm $^{-3}$	$10^{-67} - 10^{25}$ cm $^{-3}$
Clustering	No	Yes
ρ_{local}	$\sim \rho_{\text{bkg}}$	0.4 GeV cm $^{-3}$
n_{local}	$\sim n_{\text{bkg}}$	$10^{-62} - 10^{30}$ cm $^{-3}$
Momentum dist.	Fermi-Dirac	?

Table 1. Properties of neutrinos and dark matter [1, 19, 20]. The lower section of the neutrino column lists the properties of cosmic relic neutrinos. For the total neutrino mass, we cite the limits from DESI baryon acoustic oscillation (BAO) + CMB, assuming the neutrino masses show the normal hierarchy [21]. The cosmic neutrino abundance and its percentage of the total mass are calculated accordingly using cosmological parameters from [10]. The number density of cosmic neutrinos are the background density and that of dark matter is the local halo density.

Below which particles should be thought as wave-like (like classical electromagnetic field) rather than particle-like. Those candidates are known as ultra-light dark matter.

What we mean by “the nature of dark matter remains elusive” is that we do not understand the properties of dark matter as well as other Standard Model particles. Tab. 1 compares dark matter to neutrinos, the least understood corner of the Standard Model. Unlike neutrinos, we still lack understanding of dark matter’s spin, number of species, and the production mechanisms. Constraints on the dark matter mass and its local number density are also much looser than those of neutrinos. We are also not sure if dark matter can be produced on Earth or far-away stars. The elusive nature of dark matter is both a challenge and an opportunity. It stimulates theorists to propose new models and enable experimentalists to invent new search schemes. Meanwhile, despite the limited understanding of dark matter, people have been using the distribution of dark matter to probe what happens in the early universe and other fundamental physics.

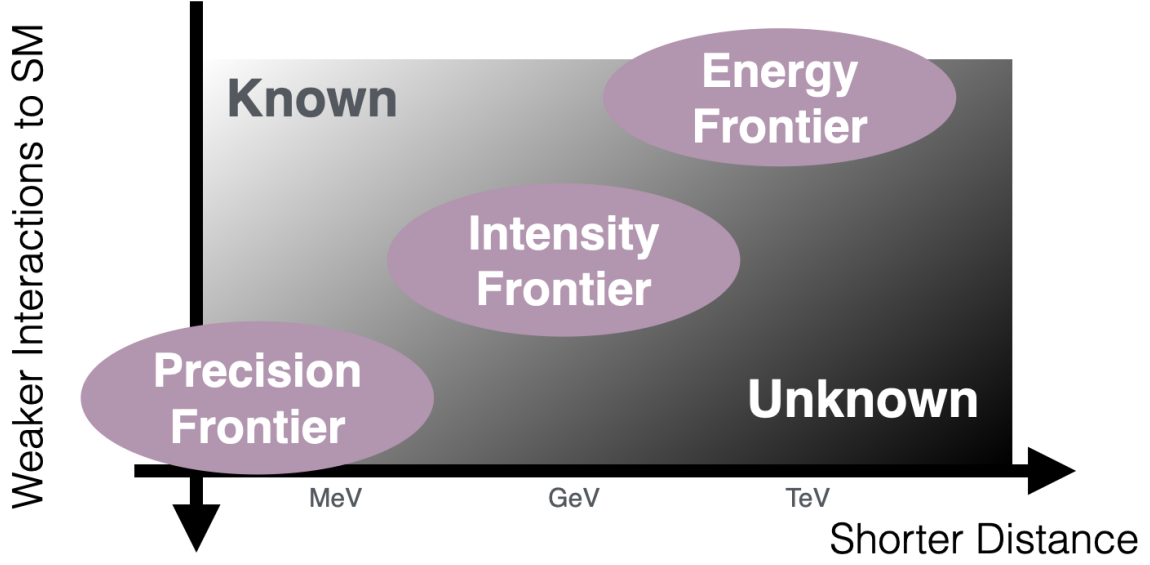


Figure 3. Frontiers in particle physics

2.3 Dark matter with dark sector mediators

The Standard Model includes numerous bosons and fermions with intricate interactions. A similar situation might occur with dark matter, potentially existing within dark sectors composed of feebly interacting particles, such as dark photons and dark Higgs bosons. The concept of dark sectors can be traced back to the hidden sectors involved in supersymmetry breaking (see review [22]) and the hidden valleys [23]. This idea gained traction when [24] employed Sommerfeld-enhanced dark matter annihilation, a phenomenon involving a light dark mediator, to explain the PAMELA positron excess [25]. Over the past decade, light dark mediators have appeared crucial in addressing numerous other puzzles, such as the muon $g-2$, neutron lifetime [26], proton charge radius [27], and the ATOMKI anomaly [28]. Among the notable examples are the “Fabulous Five”:²

- Dark photon A' ,
- Dark Higgs S ,
- Axion-like particle a ,
- Sterile neutrino N
- Millicharged particle³.

Their interactions with the Standard Model sector occur through various “portal” interactions:

- Vector portal with kinetic mixing: $\epsilon F_{\mu\nu} F'^{\mu\nu}$

²Source: Prof. Lian-Tao Wang

³The millicharged particle can be considered a new particle coupled to a massless dark photon

- Vector portal with $U(1)_{B-L}$: $A'_\mu J_{B-L}^\mu$
- Higgs portal: $H^\dagger H(\lambda S^2 + AS)$
- Neutrino portal: LHN
- Axion portal: $\frac{1}{f} \partial_\mu a J_A^\mu$
- ...

I believe the growing interest in dark sector particles and portal interactions signifies a paradigm shift in the particle physics community. This new perspective acknowledges that new physics can occur at both higher and lower energies. Consequently, we should fully leverage available facilities and technologies to explore light new physics. This shift is evident in the blooming of intensity frontier experiments, such as flavor factories, fixed-target experiments, muon experiments, and neutrino experiments, as well as precision frontier experiments, including the muon $g - 2$, electron EDM, and axion searches.

2.4 Complementarity of different probes

Let us consider a concrete example to illustrate the complementarity of different probes for the dark sector and dark matter. We take the dark matter candidate to be a Dirac fermion χ , with the scalar mediator S coupling only to Standard Model leptons.

$$\mathcal{L} \supset -g_\chi S \bar{\chi} \chi - \sum_{\ell=e,\mu,\tau} g_\ell S \bar{\ell} \ell. \quad (2.5)$$

We will assume that both S and χ are light, with masses below $\mathcal{O}(10)$ GeV, and that S is *real*. The couplings of S to leptons can be understood as originating from the effective gauge-invariant dimension-5 operators:

$$\frac{c_i}{\Lambda} S \bar{L}_i H E_i. \quad (2.6)$$

Here, Λ is the associated scale of new physics and c_i is a Wilson coefficient for flavor i . We will assume that the couplings are diagonal in the mass basis. While the relative sizes of the Wilson coefficients c_i (and hence the effective couplings g_i) are undetermined *a priori*, a natural expectation might be that they are proportional to the corresponding Yukawa coupling y_i , so that the effective g_i are proportional to the corresponding lepton masses after electroweak symmetry breaking, i.e.,

$$g_e : g_\mu : g_\tau = m_e : m_\mu : m_\tau. \quad (2.7)$$

This is the case in the framework of Minimal Flavor Violation (MFV). For Wilson coefficients $c_\ell \sim \mathcal{O}(1) \times y_\ell$ in Eq. (2.6), new physics scales $\Lambda \gtrsim 1$ TeV correspond to muon couplings $g_\mu \lesssim \mathcal{O}(10^{-4} - 10^{-3})$.

The S -lepton couplings in (2.5) also introduce effective scalar couplings to pairs of vector bosons (SVV) at one-loop. For a light scalar with mass below the electroweak scale, the most relevant SVV coupling is the scalar-diphoton coupling ($S\gamma\gamma$). This interaction is

important when the decays of $S \rightarrow \ell^+ \ell^-$ are kinematically forbidden. The interactions can be described by an effective Lagrangian,

$$\mathcal{L} \supset -\frac{1}{4}g_{\gamma\gamma}SF_{\mu\nu}F^{\mu\nu}, \quad g_{\gamma\gamma} = \frac{\alpha}{2\pi} \left| \sum_{\ell=e,\mu,\tau} \frac{g_\ell}{m_\ell} F_{1/2} \left(\frac{4m_\ell^2}{p_S^2}, \frac{q^2}{4m_\ell^2} \right) \right|, \quad (2.8)$$

where α is the electromagnetic fine structure constant and $F_{1/2}$ is a form factor that depends on the four-momentum-square of one of the photons (q^2) and the scalar S (p_S^2). See [29] for more details.

Turning our attention to dark matter, there are three distinct possibilities for the relative sizes of m_χ and m_S , each carrying different phenomenological consequences:

- $m_\chi < m_S/2$: In this case, if $g_\chi \gtrsim g_{e,\mu,\tau}$, the mediator S will primarily decay invisibly to $\chi\bar{\chi}$. The thermal freeze-out relic abundance of dark matter is driven by s -channel annihilation into leptons, $\bar{\chi}\chi \rightarrow \bar{\ell}\ell$ (or $\gamma\gamma$) in the early Universe. The annihilation rate is roughly given by

$$\langle\sigma v\rangle = 2\pi \frac{\alpha_D \alpha_\ell}{m_\chi} \frac{(m_\chi^2 - m_\ell^2)^{3/2}}{(m_S^2 - 4m_\chi^2)^2} \langle v_{\text{rel}}^2 \rangle, \quad (2.9)$$

where $\alpha_{D(\ell)} \equiv g_{D(\ell)}^2/(4\pi)$ and $\langle v_{\text{rel}}^2 \rangle$ is the thermal average of the relative dark matter velocity squared, reflecting the fact that annihilation is a p -wave process in this scenario. To get p -wave annihilation motivates choosing a scalar mediator with a Dirac fermion dark matter.

Why do we prefer p -wave annihilation? Observations of the CMB constrain the amount of energy injected into the Intergalactic Medium (IGM) through dark matter annihilation at late times, which can distort the CMB. However, this is only an issue if the dark matter annihilation cross-section is s -wave [30–32]. A p -wave annihilation cross-section can effectively evade these CMB constraints.

- $m_S/2 \lesssim m_\chi \lesssim m_S$: In this case, s -channel annihilation into leptons again sets the relic abundance of χ , providing a thermal relic target. However, $S \rightarrow \chi\bar{\chi}$ decays are kinematically forbidden, so S will decay visibly. This significantly changes the constraints and prospects for detection at accelerator experiments, which have been discussed in detail elsewhere.
- $m_S < m_\chi$: In this case, S decays visibly. However, annihilation in the early Universe will primarily proceed through secluded annihilation, $\bar{\chi}\chi \rightarrow SS$. The cross-section for this process only depends on the dark sector coupling g_χ , so there is no well-defined thermal relic target for terrestrial experiments.

Here we focus on the scenario with $m_\chi < m_S/2$, since it provides concrete thermal targets and is generally difficult to test, given the invisible decays of S . Fig. 4 from Ref. [29] presents various constraints on the dark scalar-Dirac dark matter model assuming $m_\chi = m_S/3$. It is a busy plot. The various shaded regions and lines indicate existing and future probes

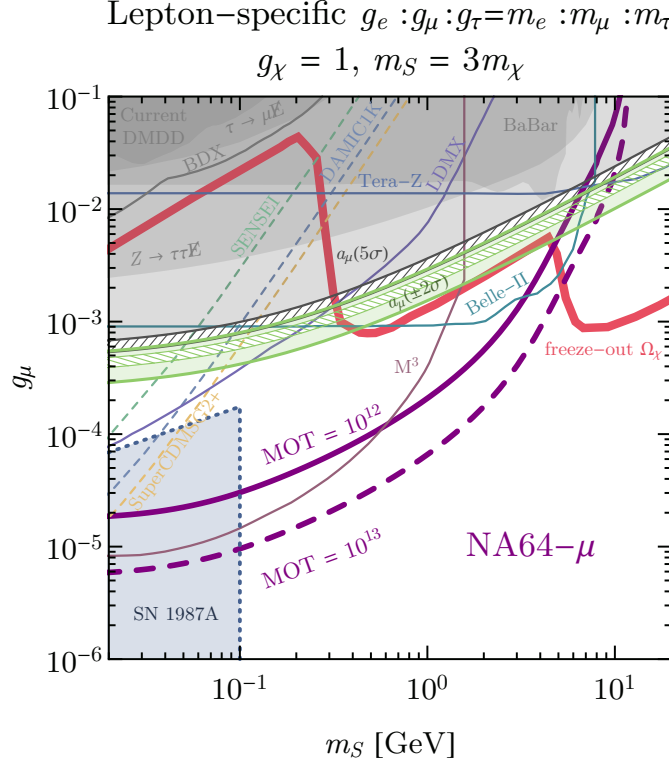


Figure 4. Current (shaded regions) and projected (lines) constraints for the dark matter-lepton-specific mediator model in the $g_\mu - m_S$ parameter space. We assume $m_\chi = m_S/3$ and $g_\chi = 1$. All the constraints are at 95% CL. The red curve indicates the parameters required to reach the correct thermal freeze-out dark matter abundance. The green and gray regions represent the 2σ -favored and 5σ -excluded regions based on current a_μ measurements. The blue region represents approximate exclusions from the cooling of SN 1987A. The shaded gray regions are limits from light dark matter direct detection experiments, XENON 10/100, DarkSide-50, and CDMS HVeV (collectively denoted as "current DMDD"), exotic Z and τ decays, and mono- γ searches at BaBar [33]. Colored lines are the sensitivity projections for NA64- μ , M^3 [34], LDMX [35], BDX [36], mono-photon searches at Belle-II [33], and Tera-Z [37], and expected DMDD limits from SENSEI, DAMIC-1K, and SuperCDMS-G2+.

of the model respectively, forming a tight complementarity for the parameter space. I will summarize the major constraints as the “floor”, the “ceiling”, and the “fence” and “walls” at the lighter end of the dark scalar/dark matter mass.

- **The floor: Relic abundance.** Regions below the red curves are excluded due to an overabundance of dark matter for the mass ratio $m_S/m_\chi = 3$. This can be understood as smaller couplings being more susceptible to the expansion of the universe, ending the freeze-out at a higher temperature. The kinks in the red curves around $m_S = 2m_\mu$ and $m_S = 2m_\tau$ occur when a new annihilation channel becomes kinematically accessible as indicated by Eq. (2.9), which allow a drop in the couplings.

Note that the constraints from the relic abundance could change dramatically by the

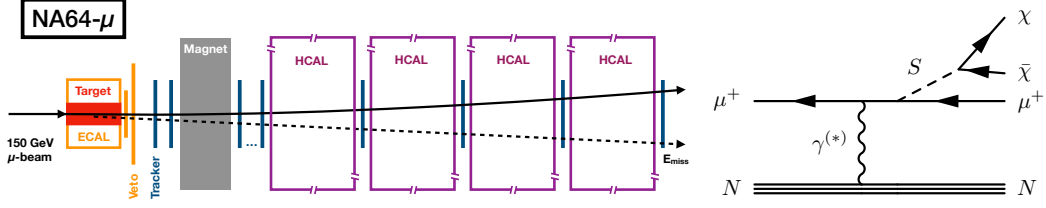


Figure 5. Left: The detector segment of the proposed NA64- μ experimental setup. Right: One diagram that leads to a muon missing momentum event.

resonant enhancement, which occurs when $m_S \approx 2m_\chi$. In such a limit, $\langle\sigma v\rangle$ can be greatly enhanced and the overabundance floor will move downward considerably. For a rough estimate, set

$$\langle\sigma v\rangle \sim 2\pi\alpha_D\alpha_\mu \frac{m_\chi^2}{m_S^2} \sim 3 \times 10^{-26} \text{ cm}^3/\text{s} = \frac{1}{(20 \text{ TeV})^2} \quad (2.10)$$

yielding $g_\mu \sim 10^{-3}$ at $m_S = 1 \text{ GeV}$ ($m_S/m_\chi = 3$, $\alpha_D = 1/4\pi$). The benchmark value $\langle\sigma v\rangle$ is derived from the observed dark matter relic abundance under the dark matter freeze-out scenario. See Appendix B.3 for more details.

- **The ceiling: Searches in collider and accelerator, rare decays.** The best way to search for light dark sector particles is through intensity frontier experiments, including fixed target experiments, rare decays, flavor factories, high-luminosity collider experiments, and neutrino experiments. Because we assume dark scalars predominantly couple to dark matter rather than Standard Model particles, which are better constrained, the signals we are looking for include missing momentum/energy, partially invisible decays, and mono-photon signals.

Take NA64- μ , the fixed-target experiment with a muon beam, as an example. The setup is shown in the left panel of Fig. 5. It shoots a 100 GeV muon beam at a lead target and looks for events with large missing momentum using the trackers and HCAL behind. If dark scalar is produced through the bremsstrahlung process $\mu N \rightarrow \mu NS(\bar{\chi}\chi)$ (right panel of Fig. 5), it will appear as a missing momentum event. The number of missing momentum events, N_χ , can be estimated as

$$N_\chi \sim N_\mu \times (n_{\text{atom}} y \sigma_{\mu N \rightarrow \mu NS}) \quad (2.11)$$

where $N_\mu = 10^{13}$ is the total number of muons on target, $n_{\text{atom}} = 10^{22} \text{ cm}^{-3}$ is the atomic number density of a lead target. y is the muon beam penetration length, which we approximate it with the target length, 20 cm. The bremsstrahlung process $\mu N \rightarrow \mu NS(\bar{\chi}\chi)$ can be treated using the improved Weizsacker-Williams approximation, which treat the virtual photon between the muon and lead atom as a real photon. Under the assumption, the cross section for $m_S \ll m_\mu$ can be estimated as

$$\sigma_{\mu N \rightarrow \mu NS} \sim \frac{\pi\alpha_\mu\alpha}{m_\mu^2} \alpha Z^2, \quad (2.12)$$

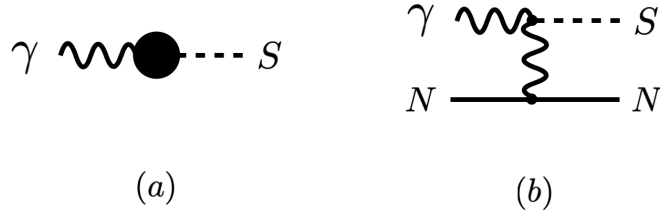


Figure 6. Process that generates dark scalars in the SN1987A. (a) resonant mixing; Note that photons in the plasma carries an in-medium mass. Its longitude mode can mix with the scalar. (b) Primakoff process.

where Z is the atomic number of the lead. The factor Z^2 comes from the elastic scattering between the muon and all protons in the atom. Requiring at least three N_χ events to be observed leads to $g_\mu \sim \mathcal{O}(10^{-5})$. A more careful analysis can be found in [29], which yields $g_\chi \sim 10^{-5}$. As the scalar mass becomes heavier, it is difficult to bremsstrahlung the heavy scalar given the energy loss of the muon beam is limited. In our case, given the energy loss per penetration length is $\mathcal{O}(10^{-2}) \text{ GeV cm}^{-1}$ and the target length is 20 cm, it will be difficult to generate scalar with mass $\gtrsim \mathcal{O}(1) \text{ GeV}$. The board range of detection sensitivity below a mass threshold is a feature of intensity experiments.

- **The left fence: SN 1987A** A crucial constraint on light scalars coupled to the Standard Model particles arises from supernova (SN) cooling. A core-collapse supernova acts like a proto-neutron star, with highly-degenerate and relativistic electrons, near-degenerate and non-relativistic nucleons, and possibly some muons [38]. It primarily cools through neutrino diffusion. The measured SN 1987A neutrino burst flux matches model predictions [39]. And the energy loss per unit mass is constrained by the Raffelt bound,

$$\epsilon_{\text{Raffelt}} = 10^{19} \text{ erg g}^{-1} \text{ s}^{-1}. \quad (2.13)$$

The SN event can constrain dark scalars and leptophilic dark matter produced through prompt decays. If g_ℓ is too small, no significant dark scalar population is produced in the SN, so S does not contribute to cooling. If g_ℓ is too large, dark matter produced via S decays is trapped inside the SN and again does not contribute to cooling.

Dark scalars with mass less than the plasma frequency of the photon, ω_p ($\simeq 20 \text{ MeV}$ for SN 1987A), can be resonantly produced through mixing with the photon's longitudinal mode [40]. See left panel of Fig. 6. Requiring the energy loss to be below this value gives an upper limit in the $m_S - g_\mu$ plane (lower edge of the excluded region) around $g_e \approx 10^{-10}$ for $m_S \lesssim 20 \text{ MeV}$ [41], translating to $g_\mu \approx 10^{-8}$. For $m_S \sim 100 \text{ MeV}$, resonant production is suppressed, but dark scalars can still be produced via continuum processes like $\gamma N \rightarrow NS$ [42]. See right panel of Fig. 6. This results in an upper limit around $g_{\gamma\gamma} \approx 6 \times 10^{-9} \text{ GeV}^{-1}$ for $m_S \lesssim 100 \text{ MeV}$ [33], translating to $g_\mu \approx \text{few} \times 10^{-7}$.

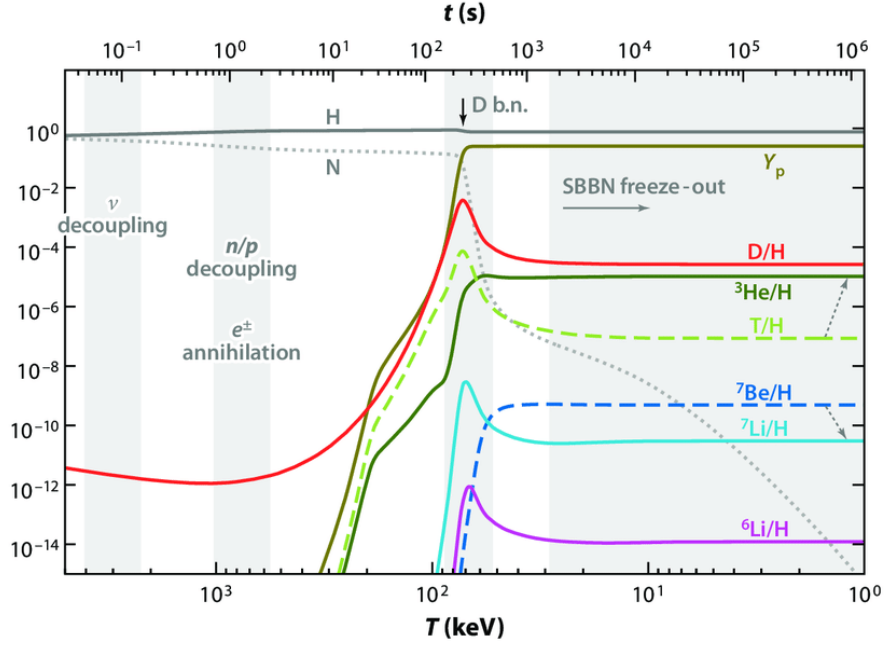


Figure 7. The evolution of the abundance of primordial elements during the standard BBN process. The gray band indicates four important stages: neutrino decoupling, n/p freeze-out and electron-positron annihilation, deuterium bottleneck, and freeze-out of all other elements. The plot is taken from [44].

Once produced in the SN, dark scalars decay into $\chi\bar{\chi}$, given $m_S > 2m_\chi$ and $g_\ell \ll g_\chi = 1$. dark matter interacts with plasma particles, such as electrons, photons, and protons, limiting dark matter outflow and setting a lower limit (upper edge of the excluded region) on g_ℓ for sufficiently light scalars produced in the SN. We use $\chi\gamma \rightarrow \chi\gamma$ interactions for preliminary constraints. For a rough estimate, adopting a mean-free-path criterion,

$$(n_\gamma \sigma_{\chi\gamma \rightarrow \chi\gamma})^{-1} \lesssim r_{\text{core}} \quad (2.14)$$

with $n_\gamma = 10^{33} \text{ cm}^{-3}$ and $r_{\text{core}} \approx 1 \text{ km}$ yields $g_\mu \sim \mathcal{O}(10^{-3})$. A more sophisticated treatment uses the “ $\pi/2$ -deflection criterion” proposed by [43], leading to $g_e \approx 5 \times 10^{-7}$, translating to $g_\mu \simeq 10^{-4}$. This increases slightly for larger m_S as heavier dark matter is more difficult to trap.

2.5 The wall: N_{eff} constraints

BBN begins when the temperature of the universe drops below $T = \mathcal{O}(1) \text{ MeV}$ and concludes around $T = 30 \text{ keV}$. The key stages of standard BBN include neutrino decoupling, n/p freeze-out, the electron-positron annihilation, and the deuterium bottle neck. Figure 7 shows the evolution of the abundance of primordial elements during the standard BBN process [44]. These theoretical predictions are tested against observations using two key observables: the primordial ^4He mass fraction, Y_p , and the ratio of the abundances of primordial deuterium and hydrogen, D/H . The theoretical predictions for the standard

BBN are [45, 46]:

$$Y_p = 0.2469 \pm 0.0002, \quad D/H = (2.506 \pm 0.110) \times 10^{-5}. \quad (2.15)$$

And the current measured values are:

$$Y_p = 0.245 \pm 0.003, \quad D/H = (2.547 \pm 0.029) \times 10^{-5}. \quad (2.16)$$

Therefore, the standard BBN model is well-supported by observational data.⁴

BBN, together with the CMB, is a crucial tool for constraining light dark matter and dark sector models, including those coupled to the Standard Model via dark mediators or pure gravity. The new physics is manifested in a quantity, N_{eff} , that relates the energy density of photons to the total radiation energy density:

$$\rho_r = \rho_\gamma \left(1 + \frac{7}{8} \left(\frac{4}{11} \right)^{1/3} N_{\text{eff}} \right) \Rightarrow N_{\text{eff}} \equiv \frac{8}{7} \left(\frac{11}{4} \right)^{4/3} \left(\frac{\rho_r - \rho_\gamma}{\rho_\gamma} \right). \quad (2.17)$$

The pre-factor $\frac{7}{8} \left(\frac{4}{11} \right)^{1/3}$ before N_{eff} is specifically designed for neutrinos, which were in thermal equilibrium with the Standard Model plasma until the weak interaction rate became smaller than the Hubble parameter around $T = \mathcal{O}(1)$ MeV. After decoupling, the cosmic neutrino relic undergoes expansion and maintains a quasi-thermal distribution with a temperature $T_\nu \propto a^{-1}$. Photons have the same scale-factor dependence, $T_\gamma \propto a^{-1}$. Without electron-positron annihilation, both fluids would share the same temperature. In the standard BBN, electron-positron annihilation occurs around $T \sim 0.5$ MeV, heating the photons and creating an interesting ratio between T_γ and T_ν .

Between neutrino decoupling and electron-positron annihilation, the total entropy degrees of freedom (dof) of the Standard Model plasma is given by (see Appendix B for more details)

$$g_{*s}(T_1) = \underbrace{2}_{\gamma\text{'s dof}} + \underbrace{\frac{7}{8}}_{\text{Fermion discount}} \left(\underbrace{2}_{e^+\text{'s dof}} + \underbrace{2}_{e^-\text{'s dof}} \right) = \frac{11}{2}. \quad (2.18)$$

After electron-positron annihilation, the total entropy dof becomes

$$g_{*s}(T_2) = \underbrace{2}_{\gamma\text{'s dof}}. \quad (2.19)$$

Entropy conservation demands

$$g_{*s}(T_1)T_1^3 = g_{*s}(T_2)T_2^3 \Rightarrow T_\nu = \left(\frac{4}{11} \right)^{1/3} T_\gamma, \quad (2.20)$$

where ν 's follow the temperature T_1 and γ 's follow the temperature T_2 . Therefore, if there are N_{eff} species of neutrinos, their contribution to ρ_r is

$$N_{\text{eff}} \times \rho_\nu = N_{\text{eff}} \times \frac{7}{8} \left(\frac{4}{11} \right)^{4/3} \times \rho_\gamma, \quad (2.21)$$

⁴Recent progress in addressing the overabundance of primordial ^7Li can be found in [45, 47].

where we use the relation

$$\rho_\gamma = 2 \times \frac{\pi^2}{30} T_\gamma^4, \quad \rho_\nu = \frac{7}{8} \times 2 \times \frac{\pi^2}{30} T_\nu^4. \quad (2.22)$$

Hence, we recover the second term in the RHS bracket of Eq. (2.17). If neutrinos decouple instantaneously, $N_{\text{eff}} = 3$ for the Standard Model. A more precise treatment of neutrino decoupling considers non-instantaneous decoupling and the process $e^+e^- \rightarrow \nu\bar{\nu}$ during electron-positron annihilation. This yields a slightly larger value [48]

$$N_{\text{eff}}^{\text{Standard Model}} = 3.044 \pm 0.0005. \quad (2.23)$$

If we have extra radiation sources besides photon and neutrinos, we can define

$$\Delta N_{\text{eff}} \equiv \rho_{\text{extra r}} / \rho_\nu \quad (2.24)$$

and simplify Eq. (2.17) into

$$N_{\text{eff}} = 3.044 + \Delta N_{\text{eff}}. \quad (2.25)$$

Observationally, N_{eff} can be constrained in two ways. The first method relies on the CMB anisotropy. It gives the ratio $f_\nu \equiv \rho_\nu / \rho_\gamma = (\rho_r - \rho_\gamma) / \rho_\gamma$ by measuring the angular size of the sound horizon θ_s and the photon diffusion length θ_d [49]. The current limit from Planck 2018 (quoted from [46]) is:

$$\Delta N_{\text{eff}}^{\text{CMB}} = 0.513. \quad (2.26)$$

Note that the above error bar is the one-sided 95% confidence level limit.

By carefully studying the nuclear reaction processes during BBN for different N_{eff} and comparing them to the observations of D/H and Y_p , an independent limit on N_{eff} can be obtained from BBN [46]:

$$\Delta N_{\text{eff}}^{\text{BBN}} = 0.407. \quad (2.27)$$

Again, the error bar is the one-sided 95% confidence level limit.

Besides CMB anisotropy and BBN, another important measurement in cosmology is that the photon temperature today, $T_{\gamma,0} = 2.73$ K, as measured by COBE/FIRAS [50]. This measurement fixes ρ_γ at higher z . Let us consider two ways a light dark matter/dark sector can modify N_{eff} :

- Adding a "sterile component". By "sterile component," I mean any new degrees of freedom that contribute to radiation and do not inject energy into the Standard Model electromagnetic sector. This can be light dark sector particles or even stochastic gravitational waves. The effect of adding sterile components is summarized in the

diagram (2.28), and is constrained by both $N_{\text{eff}}^{\text{CMB}}$ and $N_{\text{eff}}^{\text{BBN}}$.

$$\begin{aligned}
& \text{Adding sterile components} \Rightarrow \rho_r \nearrow \Rightarrow N_{\text{eff}}^{\text{CMB}} \nearrow \\
& \quad \downarrow \\
& \quad H \nearrow \Rightarrow \text{Less time to burn D} \Rightarrow \text{D/H} \nearrow \\
& \quad \downarrow \\
& \quad \text{High } n/p \text{ freeze-out temperature} \\
& \quad \downarrow \\
& \quad Y_p \nearrow
\end{aligned} \tag{2.28}$$

Consider a dark sector with dark photon A' and Dirac fermion χ . It interacts with the Standard Model sector purely gravitationally and conserves their entropy separately as they cool. We then have the following relation at a lower energy,

$$a_{\text{UV}}^3 g_{\text{Standard Model}}^{\text{UV}} T_{\gamma}^{\text{UV}^3} = a_{\text{IR}}^3 g_{\text{Standard Model}}^{\text{IR}} T_{\gamma}^{\text{IR}^3}, \quad a_{\text{UV}}^3 g_{\text{D}}^{\text{UV}} T_{\text{D}}^{\text{UV}^3} = a_{\text{IR}}^3 g_{\text{D}}^{\text{IR}} T_{\text{D}}^{\text{IR}^3} \tag{2.29}$$

which can be combined into

$$\left(\frac{T_{\text{D}}}{T_{\gamma}}\right)_{\text{IR}} = \left(\frac{g_{\text{Standard Model}}^{\text{IR}}}{g_{\text{Standard Model}}^{\text{UV}}} \frac{g_{\text{D}}^{\text{UV}}}{g_{\text{D}}^{\text{IR}}}\right)^{1/3} \left(\frac{T_{\text{D}}}{T_{\gamma}}\right)_{\text{UV}}. \tag{2.30}$$

Therefore, the energy density for the dark sector is given by

$$\rho_{\text{D}}^{\text{IR}} = g_{\text{D}}^{\text{IR}} \frac{\pi^2}{30} (T_{\text{D}}^{\text{IR}})^4 = g_{\text{D}}^{\text{IR}} \frac{\pi^2}{30} \left(\frac{g_{\text{Standard Model}}^{\text{IR}}}{g_{\text{Standard Model}}^{\text{UV}}} \frac{g_{\text{D}}^{\text{UV}}}{g_{\text{D}}^{\text{IR}}}\right)^{4/3} \left(\frac{T_{\text{D}}}{T_{\gamma}}\right)_{\text{UV}}^4 (T_{\gamma}^{\text{IR}})^4. \tag{2.31}$$

Consider the UV is when all Standard Model particles are in the plasma and the IR is before the neutrino decouples. Therefore, we have $g_{\text{Standard Model}}^{\text{UV}} = 106.75$ and $g_{\text{Standard Model}}^{\text{IR}} = 10.75$. For the dark sector, assume $g_{\text{D}}^{\text{UV}} = g_{\text{D}}^{\text{IR}} = g_{\text{D}}$ and that the two sectors have the same temperature at UV $T_{\text{D}}^{\text{UV}} = T_{\gamma}^{\text{UV}}$. This yields

$$\rho_{\text{D}}^{\text{IR}} = g_{\text{D}}^{\text{IR}} \frac{\pi^2}{30} \times 0.047 \times (T_{\gamma}^{\text{IR}})^4 \Rightarrow \Delta N_{\text{eff}} = \frac{\rho_{\text{D}}^{\text{IR}}}{\rho_{\nu}} = 0.027 g_{\text{D}}. \tag{2.32}$$

The degrees of freedom of our dark sector is

$$g_{\text{D}} = 3 + \frac{7}{8}(2 + 2) = \frac{13}{2} \Rightarrow \Delta N_{\text{eff}} = 0.174. \tag{2.33}$$

Such a dark sector is still allowed by current measurements of $N_{\text{eff}}^{\text{CMB}}$ and $N_{\text{eff}}^{\text{BBN}}$. If we allow asymmetric reheating such that $T_{\text{D}} < T_{\gamma}$ at UV, ΔN_{eff} can be further suppressed by $(T_{\text{D}}/T_{\gamma})^4$ and it is easier to escape the N_{eff} constraint.

- A more interesting scenario considers dark sector particles contributing to the electromagnetic sector before BBN. Let's consider a dark matter particle χ with mass $m_{\chi} > m_e$, which can annihilate into e^+e^- via a dark photon. In this scenario, χ will

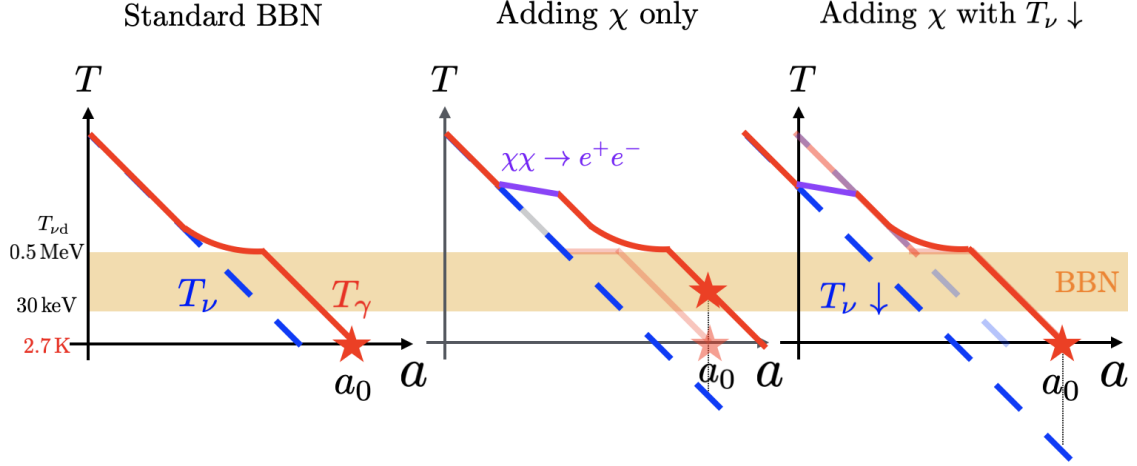


Figure 8. The evolution of the temperature of the neutrino sector T_ν and the Standard Model electromagnetic sector T_γ from before neutrino decoupling to today. Left panel: the evolution in the standard BBN, where T_γ is heated by $(11/4)^{1/3}$ due to electron-positron annihilation. The red star indicates $T_{\gamma,0}$, fixed at 2.7 K. Middle panel: adding χ that contributes to $\chi\chi \rightarrow e^+e^-$. This further heats the Standard Model electromagnetic sector, leading to a higher $T_{\gamma,0}$ than observed. Right panel: to accommodate χ , we need to lower the neutrino temperature so that $T_{\gamma,0} = 2.7$ K.

be in chemical equilibrium with the Standard Model electromagnetic sector at high temperatures. The electromagnetic sector would be heated by $\chi\chi$ annihilation when the temperature drops below m_χ . However, this is forbidden as it would lead to a CMB temperature today, $T_{\gamma,0}$, greater than 2.73 K, as shown in the middle panel of Fig. 8.

To accommodate the introduction of χ , we must lower the Standard Model sector temperature before the neutrino decoupling. This results in a smaller neutrino sector temperature and restores $T_{\gamma,0}$ to the measured value. As summarized in diagram (2.34), there are still two consequences: the lower T_ν leads to lower radiation ρ_r and a lower Hubble parameter during BBN, resulting in a lower $N_{\text{eff}}^{\text{CMB}}$ and lower D/H . The slower expansion of the universe allows more time for freeze-out and burns more D into heavier elements. Interestingly, Y_p is affected by two opposing factors: the lower n/p freeze-out temperature and a smaller n/p interconversion rate induced by the colder neutrino [51]. The net effect is that Y_p remains almost unchanged

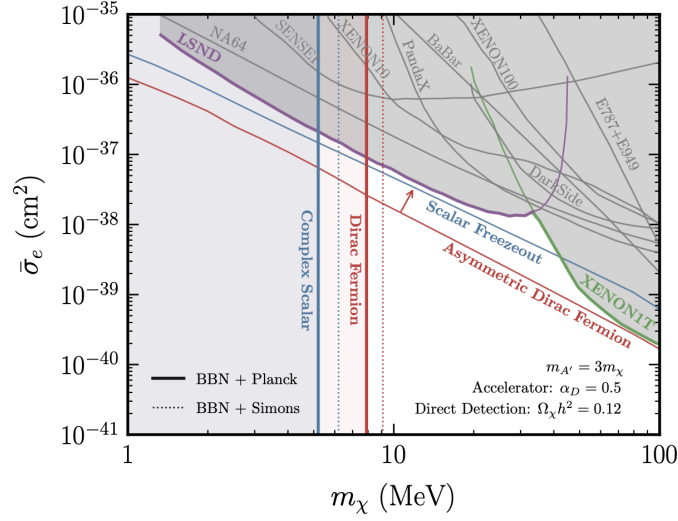


Figure 9. The constraints from N_{eff} of BBN + CMB on dark photon-dark matter model. The plot is taking from [52].

compared to standard BBN.

Add χ ($\chi\chi \rightarrow e^-e^+$) \Rightarrow electromagnetic sector would be heated, but $T_{\gamma,0}$ is fixed

$$\begin{aligned}
& \Uparrow \\
& T_\nu \searrow \\
& \Downarrow \\
& \rho_r \searrow \Rightarrow N_{\text{eff}}^{\text{CMB}} \searrow \\
& \Downarrow \\
& H \searrow \Rightarrow \text{More time to burn D} \Rightarrow \text{D/H} \searrow \\
& \Downarrow \\
& \text{Lower } n/p \text{ freeze-out temperature} \\
& \text{But } T_\nu \searrow \Rightarrow \text{Less } n/p \text{ interconversion rate} \\
& \Downarrow \\
& Y_p \text{ unchanged}
\end{aligned} \tag{2.34}$$

One may think to hide the extra annihilation by adding a sterile components. In this case, the changes in $N_{\text{eff}}^{\text{CMB}}$ and D/H cancel. However, the enhancement in Y_p cannot be mitigated unless additional new physics is introduced. See diagram (2.35). Since Y_p alone is well-measured, we still have strong constraints on χ .

$$\begin{aligned}
& \text{Add } \chi \text{ } (\chi\chi \rightarrow e^-e^+) \text{ and sterile components } \Rightarrow N_{\text{eff}}^{\text{CMB}} \text{ unchanged} \\
& \Downarrow \\
& \text{D/H unchanged, but } Y_p \nearrow
\end{aligned} \tag{2.35}$$

The quantitative analysis of the extra annihilation scenario and the combined scenario requires implementing the nuclear reaction processes using BBN codes, such as ACROPOLIS [53], ALTERBBN [54], PRIMAT [55, 56], and PRYMORDIAL [57]. Ref. [52] uses a modified PRIMAT code to set $m_\chi > 5.2(7.9)$ MeV for dark matter to be a complex scalar (Dirac fermion), assuming $m_{A'}/m_\chi = 3$. This is shown as the left walls in Fig. 9. The bound is valid as long as the coupling between the dark matter and the Standard Model sector is large enough to bring $\chi\chi \leftrightarrow e^+e^-$ to chemical equilibrium when $T_\gamma \gtrsim m_{A'}$, i.e., $(\Gamma_{\chi\chi \leftrightarrow e^+e^-} = H)_{T_\gamma=m_{A'}}$. The result corresponds to $\bar{\sigma}_e \equiv \frac{16\pi\alpha_D\epsilon^2\mu_{\chi e}^2}{(\alpha^2 m_e^2 + m_{A'}^2)^2} \gtrsim 10^{-43} \text{ cm}^2$.

3 Second lecture

There are not so many trending dark matter models in the astrophysics community. Besides CDM, people often consider

- Warm dark matter
- Fuzzy dark matter, a.k.a ultralight dark matter
- Self-interacting dark matter
- Interacting dark matter

WDM primarily affects the halo mass function. FDM also alters the halo mass function but, in addition, leads to very different dark matter density profiles within the halos. SIDM does not modify the halo mass function, but it results in dynamically evolving dark matter density profiles within the halos. Interacting dark matter (IDM) involves strong interactions with baryons, with cross-sections surpassing those of dark matter overbunden. IDM can produce a halo mass function similar to WDM, along with additional features such as dark acoustic oscillations. There are also models that combine features from the above baseline models. An example is atomic dark matter, which consists of dark electrons, dark protons, and dark photons. Its phenomenology exhibits characteristics of WDM, SIDM, and IDM.

The popularity of these models is due to two main reasons. Firstly, dark matter on a large scale is well-constrained and is expected to be CDM-like. Consequently, significant deviations are anticipated only in the small-scale structures (dark matter halos). Secondly, astrophysical and cosmological studies often require extensive numerical simulations. Thus, models with a single parameter, such as dark matter mass for WDM and FDM or cross-section strength for SIDM, are ideal. However, new techniques like machine learning may eventually allow us to thoroughly explore models with multiple parameters, such as IDM and atomic dark matter.

In the following sections, we will discuss two aspects of non-CDM imprints on small-scale structures: the effects on structure formation, which influence the distribution of halos of various masses, and the effects on a single halos' density profiles.

3.1 Small-scale power spectrum: probing dark matter in the early universe

Our universe today is full of matter-rich halos and matter-poor voids, which developed from small initial overdensities (and underdensities) in the primordial matter distribution, potentially originated from the quantum fluctuations through inflation. These overdensities, denoted by

$$\delta_m(\mathbf{x}) \equiv \frac{\rho_m(\mathbf{x}) - \bar{\rho}_m}{\bar{\rho}_m}, \quad (3.1)$$

where $\bar{\rho}_m$ is the averaged matter density, grow over time due to gravity. To be more specific, they first grew in the linear perturbation regime, where $\delta_m \ll 1$, as the long-wavelength modes re-entered the horizon. As these overdensities evolved, they entered the non-linear regime ($\delta_m > 1$), leading to the collapse of surrounding background dark matter and the formation of virialized halos. The average density of a dark matter halo is approximately $\Delta_h = 200$ times the background density. Smaller halos merged or accreted matter to form larger ones, a process manifested in the halo mass-redshift relation and the concentration-halo mass-redshift relation, with concentration indicating how compact a halo is.

In practice, we use “two-point statistics,” such as the matter power spectrum and the halo mass function, to characterize the distributions of overdensities and halos. These tools are important for studying the properties of dark matter and beyond. While observations on large scales generally support the predictions of the Λ CDM model, there can be significant deviations on smaller scales. Additionally, observations of galaxies and dwarf galaxies have raise several difficult questions for Λ CDM, such as the diversity of rotation curves and the too-big-to-fail problem, suggest the need for dark matter models beyond CDM.

It is better to Fourier transform the overdensity from the position space to the momentum space

$$\delta_m(\mathbf{x}) = \int d^3k \delta_m(\mathbf{k}) e^{-i\mathbf{k}\cdot\mathbf{x}} \quad (3.2)$$

where \mathbf{k} is the 3D momentum vector. The matter power spectrum is related to the two-point correlation function of $\delta_m(\mathbf{k})$ by

$$\langle \delta_m(\mathbf{k}) \delta_m(\mathbf{k}') \rangle = (2\pi)^3 \delta^3(\mathbf{k} + \mathbf{k}') P_m(k) \quad (3.3)$$

where $\langle \dots \rangle$ averages over all the spacial configurations and P_m is only a function of the magnitude of \mathbf{k} due to the cosmological principle. Often it is convenient to introduce dimensionless matter power spectrum $\Delta^2(k)$ that relates to $P_m(k)$ by

$$\Delta^2(k) \equiv \frac{k^3 P_m(k)}{2\pi^2}. \quad (3.4)$$

Fig. 10 (Fig. 11) shows the (dimensionless) linear matter spectrum at $z = 0$ for the CDM, WDM, Fuzzy dark matter, and interacting dark matter, along with observations from CMB and LSS. As is common in astronomical plots, the data should be read from right to left. Modes with smaller wavenumbers enter the horizon earlier than those with larger wavenumbers. Let’s focus on the CDM prediction first, which sets the baseline of the matter power spectrum that agrees well with observations at $k \lesssim 10 h \text{ Mpc}^{-1}$.

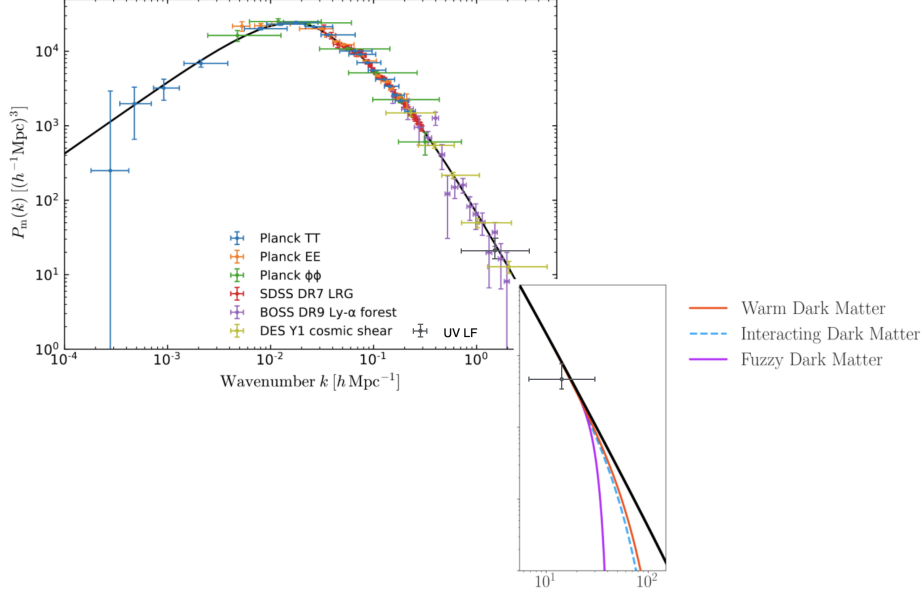


Figure 10. Linear matter power spectrum at $z = 0$, reproduced from Nadler’s BCCP seminar slides [58]. We added constraints from the ultraviolet galaxy luminosity-function (UV LF) [59]. The measured data are complied by [60]. From the largest scales to smaller ones, the data includes Planck CMB, galaxy clustering, galaxy weak lensing, Ly- α clustering, and UV LF.

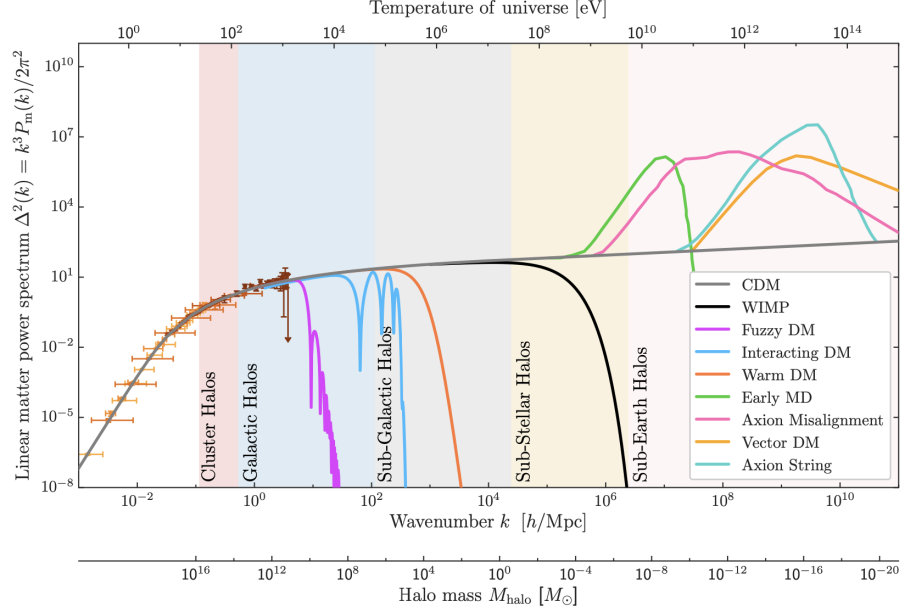


Figure 11. Dimensionless linear matter power spectrum at $z = 0$, reproduced from [61]. Detailed explanation of model predictions can be found in [61]. The measured data are complied by [60].

3.1.1 The power spectrum of CDM

A notable feature of the CDM power spectrum is the turnover around $k = 0.02 h \text{ Mpc}^{-1}$. This scale corresponds to modes entering the horizon at the matter-radiation equality,

denoted as k_{eq} . For modes with wavenumber $k < k_{\text{eq}}$, the power spectrum behaviors as $P_{\text{m}}(k) \propto k$. For modes with wavenumber $k > k_{\text{eq}}$, the relationship changes to $P_{\text{m}}(k) \propto k^{-3}$. In the dimensionless spectrum, where $P_{\text{m}}(k)$ is multiplied by k^3 , we find $\Delta^2(k) \propto k^4$ for $k < k_{\text{eq}}$ and $P_{\text{m}}(k)$ exhibits a logarithmic-like growth with respect to k for $k > k_{\text{eq}}$.

This behavior can be well explained using linear perturbation theory. A more detailed and comprehensive derivation can be found in works such as [3], which starts by perturbing a set of fluid dynamics equations:

$$\frac{\partial \rho}{\partial t} + \nabla \cdot (\rho \mathbf{u}) = 0, \quad \frac{\partial \mathbf{u}}{\partial t} + (\mathbf{u} \cdot \nabla) \mathbf{u} = -\nabla \Phi - \frac{\nabla P}{\rho}, \quad \nabla^2 \Phi = 4\pi G \rho. \quad (3.5)$$

where \mathbf{u} is the velocity of the fluid and Φ is the gravitational potential. Here, we simplify the derivation by directly introducing the resulting master equation:

$$\frac{d^2 \delta_{\text{m}}}{dt^2} + 2H \frac{d\delta_{\text{m}}}{dt} = 4\pi G \bar{\rho}(t) \delta_{\text{m}}, \quad (3.6)$$

where we assume that the matter has zero pressure and all the matter clumps. Although this assumption is not entirely accurate, it is not far off and simplifies our derivation. Let's use the ansatz

$$\delta_{\text{m}}(\mathbf{k}, t) = \delta_+(\mathbf{k}) D_+(t) + \delta_-(\mathbf{k}) D_-(t), \quad (3.7)$$

to separate the \mathbf{k} -dependent and t -dependent parts of δ_{m} . The subscript $+$ refers to the growing mode and $-$ to the decaying mode. We will focus on the growing mode.

In the matter era, we have $a \propto t^{2/3}$, $H = 2/(3t) \propto a^{-3/2}$, and $4\pi G \bar{\rho}_{\text{m}}(t) = 3H^2/2 = 2/(3t^2)$ (see Tab. 4 for a summary). Substituting those relations to Eq. (3.6) yields

$$\frac{d^2 D}{dt^2} + \frac{4}{3t} \frac{dD}{dt} = \frac{2}{3t^2} D \quad \Rightarrow \quad D(t) = c_1 t^{-1} + c_2 t^{2/3} \quad (3.8)$$

Therefore the growing mode gives $D_+ \propto t^{2/3} \propto a$.

In the radiation era, the scale factor behaves as $a \propto t^{1/2}$ and the Hubble parameter is given by $H = 1/(2t) \propto a^{-2}$. In such a universe,

$$\ddot{\delta}_{\text{m}} \sim H \dot{\delta}_{\text{m}} \sim H^2 \delta_{\text{m}} \sim 4\pi G(\bar{\rho}_{\text{r}} + \bar{\rho}_{\text{m}}) \delta_{\text{m}} \gg 4\pi G \bar{\rho}_{\text{m}} \delta_{\text{m}}, \quad (3.9)$$

so the right-hand side of Eq. (3.6) can be approximated as zero:

$$\frac{d^2 D}{dt^2} + 2H \frac{dD}{dt} = 0 \quad \Rightarrow \quad D(t) = c_1 + c_2 \ln t. \quad (3.10)$$

Therefore, the growing mode gives $D_+ \propto \ln t \propto \ln a$.

Subhorizon fluctuations in the radiation era only grow logarithmically, $\delta_{\text{m}} \sim \text{const}$, while in the matter era, the growth accelerates to $\delta_{\text{m}} \propto a$. This difference in growth rates leads to the k -dependence in the matter power spectrum. This is because different k -modes cross the horizon at different times in different eras, experiencing different subhorizon growth.

Let's assume the initial matter power spectrum is scale-invariant, i.e.,

$$(k^3 P_{\text{m}})_i = \text{const}. \quad (3.11)$$

Modes outside the horizon always have the same shape as the initial spectrum. Now consider modes crossing the horizon during the matter era, their amplitudes grow by a_0/a_h , where a_h is the scale factor at horizon crossing. In the matter era, a_h is determined by

$$k = a_h H(a_h) \propto a_h a_h^{-3/2} \Rightarrow a_h \propto k^{-2} \quad (3.12)$$

Therefore, the power spectrum is scaled as

$$k^3 P_m \propto \left(\frac{a_0}{a_h}\right)^2 (k^3 P_m)_i \propto k^4 \quad (3.13)$$

For modes crossing the horizon during the radiation era, their amplitudes grow by $\ln(a_{\text{eq}}/a_h)$. a_h in the radiation era is given by

$$k = a_h H(a_h) \propto a_h a_h^{-2} \Rightarrow a_h \propto k^{-1}. \quad (3.14)$$

This leads to the power spectrum scaling

$$k^3 P_m \propto \left(\ln \frac{a_{\text{eq}}}{a_h}\right)^2 (k^3 P_m)_i \propto \left(\ln \frac{k}{k_{\text{eq}}}\right)^2 \quad (3.15)$$

Note that when those modes later involves in the matter era, their amplitude will be enhanced by a common factor which does not affect the shape of the spectrum. Combing the above results, we have the k -dependence

$$P_m(k) \propto \begin{cases} k & k < k_{\text{eq}}, \\ k^{-3} \left(\ln \frac{k}{k_{\text{eq}}}\right)^2 & k > k_{\text{eq}}. \end{cases} \quad (3.16)$$

The evolution of the power spectrum's shape for different cosmological era is depicted in Fig. 12

3.1.2 The power spectrum of dark matter beyond CDM

Many dark matter models beyond CDM can suppress the power spectrum at small scales for various reasons. Since the matter power spectrum $P_m(k)$ is related to the halo mass function $\frac{dN}{dM_h}(M_h)$, by carefully observing galaxies and dwarf galaxies, we have an opportunity to detect deviations from the CDM model and learn more about the properties of dark matter. Since the small-scale structures began to grow in the radiation era, new physics that suppress them should be active during the period. Therefore, the small-scale structure is an opportunity to probe dark matter in the early universe. Now let's focus on a few examples:

1. Warm Dark Matter (WDM): The comoving wavelength for free-streaming is given by

$$\lambda_{\text{fs}} = \int_{t_i}^{t_{\text{eq}}} dt \frac{v(t)}{a(t)}, \quad k_{\text{fs}} = \frac{2\pi}{\lambda_{\text{fs}}} \quad (3.17)$$

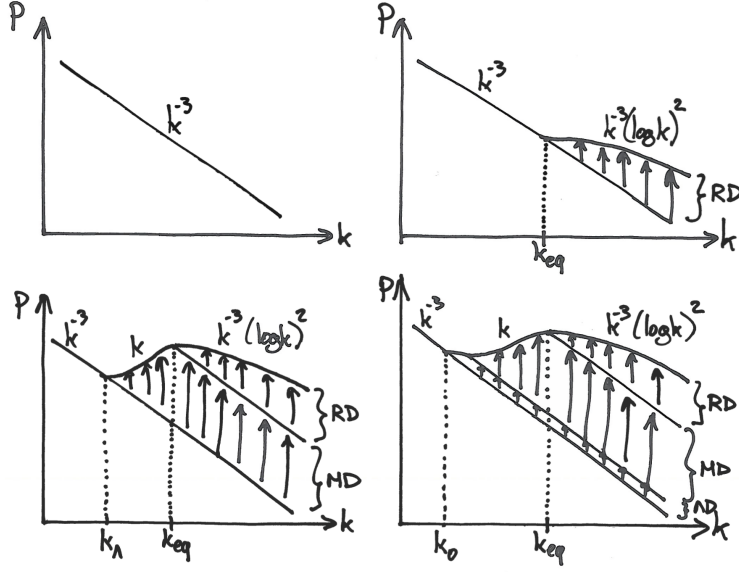


Figure 12. How the shape of the matter power spectrum involves with time. The four panel corresponds to the initial spectrum, the spectra at the radiation era, matter era, and dark energy era, respectively. The figure is taken from [62].

Note that the integral extends from an initial time t_i to the matter-radiation equality. Beyond the matter-radiation equality, the Jeans' length drops dramatically and perturbations could collapse under gravity. A crude estimation finds [63]

$$\lambda_{\text{fs}} = \int_0^{t_{\text{NR}}} dt \frac{c}{a(t)} + \int_{t_{\text{NR}}}^{t_{\text{eq}}} dt \frac{ca_{\text{NR}}}{a^2(t)} = r_{\text{H}}(t_{\text{NR}}) \left(1 + \frac{1}{2} \ln \frac{t_{\text{eq}}}{t_{\text{NR}}} \right) \quad (3.18)$$

where $r_{\text{H}}(t_{\text{NR}})$ is the comoving size of the horizon at t_{NR} . The WDM moves at the speed of light before t_{NR} and slows down as a^{-1} between t_{NR} and t_{eq} . Choosing t_{NR} to be the temperature $T_{\text{WDM}} = m_{\text{WDM}}/3$ yields

$$\lambda_{\text{fs}} = 0.4 \left(\frac{m_{\text{WDM}}}{\text{keV}} \right)^{-4/3} \left(\frac{\Omega_{\text{WDM}} h^2}{0.135} \right)^{1/3} h^{-1} \text{Mpc}. \quad (3.19)$$

This free-streaming wavelength sets a cutoff for the halo mass:

$$M_{\text{cut}} = \frac{4\pi}{3} \rho_{\chi,0} \left(\frac{\pi}{k_{\text{fs}}} \right)^3. \quad (3.20)$$

Below this cutoff, we do not expect to observe any halos for the given WDM.

However, WDM may affect the properties of halos with masses above M_{cut} , causing a departure from the observed halo mass distributions. This is because large halos grow out of smaller halos according to hierarchical structure formation, and hence will be impacted by the washout of the small halos. The halo mass function is closely related to the matter power spectrum. However, the mapping is non-trivial, and one needs

to run cosmological simulations. Based on simulation results, Ref. [64, 65] finds that the power spectrum of WDM relative to CDM is given by

$$\frac{P_{\text{WDM}}(k)}{P_{\text{CDM}}(k)} = [1 + (\alpha k)^{2\nu}]^{-\frac{10}{\nu}}, \quad (3.21)$$

with $\nu = 1.12$ and

$$\alpha = 0.049 \left(\frac{m_{\text{WDM}}}{\text{keV}} \right)^{-1.11} \left(\frac{\Omega_{\text{WDM}}}{0.25} \right)^{0.11} \left(\frac{h}{0.7} \right)^{1.22} h^{-1} \text{Mpc}, \quad (3.22)$$

where m_{WDM} and Ω_{WDM} are the WDM mass and abundance, respectively. Also note that

$$\frac{P_{\text{beyond CDM}}(k)}{P_{\text{CDM}}(k)} = [1 + (\alpha k)^\beta]^\gamma, \quad (3.23)$$

is the common functional form used to simulate cosmology for beyond-CDM dark matter.

2. Fuzzy dark matter: FDM is naturally associated with the de Broglie wavelength scale,

$$\lambda_{\text{dB}} = \frac{\hbar}{mv}. \quad (3.24)$$

This scale is linked to the soliton size at the center of an FDM halo. Since we are interested in the gravitational instability scale and halo mass cutoff of FDM, it is better to look at the Jeans scales of FDM. This starts from the fluid description of FDM, also known as the Madelung equations [66],

$$\frac{\partial \rho}{\partial t} + \nabla \cdot (\rho \mathbf{u}) = 0, \quad \frac{\partial \mathbf{u}}{\partial t} + (\mathbf{u} \cdot \nabla) \mathbf{u} = -\nabla \Phi + \frac{\hbar^2}{2m^2} \nabla \left(\frac{\Delta \sqrt{\rho}}{\sqrt{\rho}} \right), \quad \nabla^2 \Phi = 4\pi G(\rho - \bar{\rho}), \quad (3.25)$$

where we assume FDM is pressureless. Perturbing these equations around a homogeneous distribution yields ($\rho = \bar{\rho}$, $\mathbf{v} = 0$, $\Phi = 0$),

$$\frac{\partial^2}{\partial t^2} \delta_{\text{m}} = 4\pi G \bar{\rho} \delta_{\text{m}} - \frac{\hbar^2}{4m^2} \Delta^2 \delta_{\text{m}} \quad (3.26)$$

This equation is similar to Eq. (3.6) except for the absence of Hubble friction and the appearance of the "quantum pressure" term. Equation Eq. (3.26) gives the dispersion relation

$$-\omega^2 = 4\pi G \bar{\rho} - \frac{\hbar^2 k^4}{4m^2}. \quad (3.27)$$

The Jeans wavelength, determined by solving $\omega^2 = 0$, is given by [17] (modes with $k > k_J$ grow exponentially).

$$\lambda_J = \frac{2\pi}{k_J} = \frac{\pi^{3/4} \hbar^{1/2}}{(G \bar{\rho}_\chi)^{1/4} m_{\text{FDM}}^{1/2}} \quad (3.28)$$

Hence the halo cutoff mass is given by

$$M_{\text{cut}} = \frac{4}{3} \pi \bar{\rho}_\chi \left(\frac{\lambda_J}{2} \right)^3 = 1.5 \times 10^7 M_\odot \left(\frac{\Omega_{\text{FDM}}}{0.27} \right)^{1/4} \left(\frac{h}{0.7} \right)^{1/2} \left(\frac{10^{-22} \text{eV}}{m_{\text{FDM}}} \right)^{3/2} \quad (3.29)$$

Similar to the WDM case, stronger constraints can be obtained by considering the departure from the CDM power spectrum, i.e., the imprint of FDM on larger halos. Analysis of the Lyman- α forest, using an emulator, constrains $m_{\text{FDM}} > 2 \times 10^{-20}$ eV [67].

3. Interacting Dark Matter: The gravitational instability scale for IDM is determined by the horizon scale at the point when dark matter and Standard Model particles kinetically decouple.

$$\lambda_{\text{kd}} = R_{\text{H}}(\mathcal{R}_{\text{kd}} = H) \quad \text{with} \quad \mathcal{R}_{\text{kd}} \simeq \frac{m_p}{m_\chi + m_p} n_p \sigma_{\chi p \rightarrow \chi p} v_{\text{rel}}. \quad (3.30)$$

For IDM, only modes with wavelength greater than λ_{kd} can gravitational collapse to form halos. In Eq. (3.30), \mathcal{R}_{kd} is the kinetic decoupling rate, and we use $\chi - p$ interactions as an example to illustrate the derivation. Similar kinetic decoupling processes apply to other dark matter-Standard Model interactions, such as $\chi - e$ interactions. For a single $2 \rightarrow 2$ elastic scattering process, the dark matter particle with velocity \mathbf{v}_χ will experience a velocity change of

$$\Delta \mathbf{v}_\chi = \frac{m_p}{m_\chi + m_p} v_{\text{rel}} \left(\hat{\mathbf{n}}_\chi - \frac{\mathbf{v}_{\text{rel}}}{v_{\text{rel}}} \right), \quad (3.31)$$

where $\hat{\mathbf{n}}_\chi$ is the direction of the scattered dark matter particle in the center-of-mass frame. The peculiar velocity of the dark matter fluid, \mathbf{V}_χ , is then given by

$$\frac{d}{dt} \mathbf{V}_\chi = n_\chi \langle \sigma_{\chi p \rightarrow \chi p} v_{\text{rel}} \Delta \mathbf{v}_\chi \rangle = -\mathcal{R}_{\text{kd}} (\mathbf{V}_\chi - \mathbf{V}_p), \quad (3.32)$$

where $\langle \cdot \rangle$ denotes averaging over all scattering angles and the velocity distributions of dark matter and protons.

The complete derivation of λ_{kd} is more complex. Dark matter and protons, initially in a fully coupled state, first thermally decouple and then kinetically decouple. During the period between thermal and kinetic decoupling, the temperature of dark matter evolves as $T_\chi \propto a^{-2}$, which differs from the Standard Model plasma's evolution $T_\gamma \propto a^{-1}$. Therefore, it is necessary to first determine the scale factor at thermal decoupling a_{td} and then link it to the scale factor at kinetic decoupling a_{kd} . For more details, see [68].

Better constraints can be obtained through cosmological simulations from the IDM initial power spectrum. However, this involves parameter scans over m_χ and $\sigma_{\chi p}$ and can be costly. An alternative way to constrain IDM is by comparing its power spectrum to that of WDM with the maximally allowed m_{WDM} . The reason such procedure is allowed is that the spectra of WDM and IDM are similar. Therefore, one can constrain IDM by requiring $P_{\text{IDM}}(m_{\text{IDM}}, \sigma_{\chi p})/P_{\text{CDM}}$ to always lie below $P_{\text{WDM}}(m_{\text{WDM}}^{\text{limit}})/P_{\text{CDM}}$. For more details, see [68].

Ref.	Data type	$m_{\text{WDM}}^{95\% \text{C.L.}}$ [keV]	h	Ω_{dm}
[69]	luminous satellite galaxies	3.26	0.67	0.265
[70]	luminous satellite galaxies	6.5	0.7	0.24
[71]	luminous satellite galaxies	2.02	0.7	0.23
[72]	stellar stream, luminous satellite galaxies	6.3	0.67	0.26
[73]	strong lensing, luminous satellite galaxies	9.7	0.7	0.24
[74]	strong lensing, luminous satellite galaxies, Lyman- α	6.733	0.7	0.25

Table 2. 95% C.L. lower limits on the WDM mass (3rd column) from MW subhalo data reported in the literature. The 2nd, 4th, and 5th columns respectively show the data type, the value of h , and the value of Ω_{dm} that was used in the derivation of the limits.

3.1.3 Observations

It is important to note that there is a correspondence between k modes and galaxy systems, which follows the relation:

$$M_{\text{h}} \sim \frac{4\pi}{3} \rho_{\text{m}} \left(\frac{\pi}{k} \right)^3 \sim 10^{10} M_{\odot} \left(\frac{10 h \text{ Mpc}^{-1}}{k} \right)^3. \quad (3.33)$$

Thus, we have three important ranges:

1. $k \sim 0.1 - 1 h \text{ Mpc}^{-1}$: galaxy cluster halos;
2. $k \sim 1 - 100 h \text{ Mpc}^{-1}$: galaxy halos;
3. $k \gtrsim 100 h \text{ Mpc}^{-1}$: completely dark halos (which cannot form galaxies).

Probing the matter power spectrum at small scales requires finding methods to robustly investigate dark matter halos at various scales. For galaxy cluster halos, we can probe them by tracing hydrogen distribution using the Lyman- α forest, where light from distant quasars is absorbed by intergalactic neutral hydrogen residing inside halos. For galaxy halos, we can infer the abundance by observing luminous Milky Way satellite galaxies through the “galaxy-halo connection”. For completely dark halos, we need to rely on other methods, such as strong gravitational lensing or stellar streams.

To showcase the potential of different probes, we present the limits on WDM inferred from various methods or their combinations in Tab. 2, and show the parameter space constraints on IDM in Fig. 13 (taken from [68]). As shown in Fig. 13, the resulting constraints from the Milky Way satellite and Lyman- α on $\sigma_{\chi p(\chi e)}$ cover a wide range of m_{χ} . It almost rules out all high values for the dark matter overburden scenario, where the null detection of dark matter in underground direct detection experiments is due to the strong interaction between dark matter and the Earth’s atmosphere and rocks. Cosmological probes complement direct detection experiments and other dark matter-dark sector probes.

3.2 Inside dark matter halos: self-interacting dark matter

CDM encountered several challenges at small scales, including the core vs. cusp problem, the diversity problem, and the too-big-to-fail problem (see review by [103]). SIDM offers a

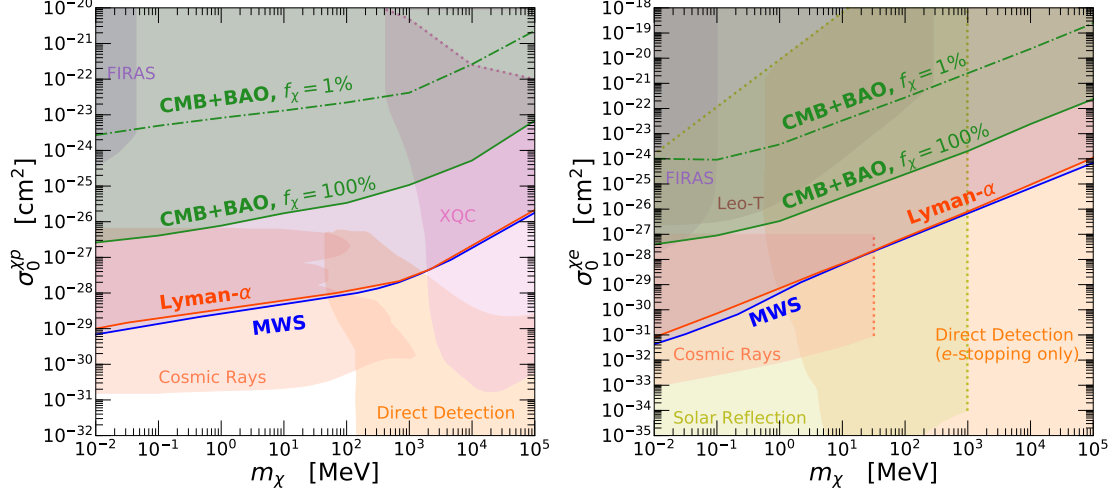


Figure 13. 95% C.L. bounds from MW subhalos (solid blue), Lyman- α forest (solid red), CMB+BAO (solid green) datasets, for velocity-independent (left) dark matter–protons and (right) dark matter–electron interactions. We also include constraints from previous literature. For dark matter–proton interactions (left): XQC rocket (pink) [75–77], various direct-detection experiments (orange: CRESST-III [78, 79], CRESST surface run [80], XENON1T [81], and Migdal effect-based EDELWEISS [82]), and cosmic-ray accelerated dark matter [83] (coral red: Mini-BOONE and XENON1T [84]; and Daya Bay and KamLAND [85]). For dark matter–electron interactions (right): gas cooling of Leo-T dwarf galaxy (brown) [86], various direct-detection experiments as considered in [87] (orange: XENON10 [88–90], XENON100 [89, 91], DarkSide-50 [92], CDMS-HVeV [93], protoSENSEI [94, 95], and SENSEI at MINOS [96]); cosmic-ray accelerated dark matter (coral red: Super-K and MiniBooNE [85, 97]), and bounds from solar reflection (yellow) [98, 99]. The dotted lines represent our conservative assumptions about the limits of the XQC (pink, with the ceiling from [76]); cosmic-ray (coral red [97]), and solar reflection (yellow [99]) bounds. In both panels: FIRAS (purple) [100–102].

common solution by providing an intrinsic mechanism for altering the dark matter distribution within halos. The core formed during the early gravothermal evolution in SIDM can address both the core vs. cusp and too-big-to-fail problems. Additionally, the super-cusp that develops in the late core-collapse stage, along with the early-stage core, may resolve the full scope of the diversity problem.

The behavior of self-interacting dark matter (SIDM) at different stages can be roughly understood using the hydrostatic equation:

$$\frac{\nabla P}{\rho} = -\nabla \Phi, \quad (3.34)$$

where $P \equiv \rho \nu^2$, ν is the velocity dispersion, and Φ is the gravitational potential. Under spherical symmetry, this equation can be rewritten as:

$$\frac{\partial(\rho \nu^2)}{\partial r} = -\frac{GM(< r)\rho}{r^2}, \quad (3.35)$$

where $M(< r)$ is the enclosed mass. Let’s consider the density profile at the time of halo formation. Since the dynamical time of a halo is typically much shorter than the SIDM

relaxation time, the density profile at halo formation can be approximated as NFW:

$$\rho(r) = \frac{\rho_s}{(r/r_s)(1 + r/r_s)^2}. \quad (3.36)$$

For the bulk of the inner halo region, the density scales as $\rho \propto r^{-1}$. Therefore, $M \propto r^2$. Assuming $\nu \propto r^s$, the left-hand side (LHS) and right-hand side (RHS) of the equation scale as:

$$\text{LHS} \propto \frac{r^{-1}r^{2s}}{r} = r^{2s-2}, \quad \text{RHS} \propto \frac{r^2r^{-1}}{r^2} = r^{-1}. \quad (3.37)$$

Requiring the LHS and RHS to have the same scaling behavior gives:

$$2s - 2 = -1 \quad \Rightarrow \quad s = \frac{1}{2}. \quad (3.38)$$

This means the halo will be cold at the center and hot at the scale radius. This temperature imbalance creates an opportunity for SIDM to manifest itself.

Next, consider the isothermal limit, where ν is independent of r . In this case, we can move ν^2 out of the partial derivative on the LHS of the equation, which can be rewritten as:

$$\frac{\partial \ln \rho}{\partial \ln r} = -\frac{GM(< r)}{r\nu^2}. \quad (3.39)$$

There are two cases to consider:

1. **Finite central value:** $\lim_{r \rightarrow 0} \rho = \rho_0$. In this case, $\lim_{r \rightarrow 0} M = \frac{4\pi}{3}\rho_0 r^3$, therefore $\lim_{r \rightarrow 0} \text{RHS} = 0$. This means the isothermal profile can have a flat core.
2. **Single power law:** $\rho = Ar^x$. Substituting this into the equation gives:

$$x = -G\frac{4\pi}{3}Ar^{x+2}\nu^{-2} \quad \Rightarrow \quad x = -2, A = \frac{3\nu^2}{2\pi G} \quad \Rightarrow \quad \rho = \frac{3\nu^2}{2\pi Gr^2}. \quad (3.40)$$

This is the so-called singular isothermal profile. Note that this is one solution but not the only solution to the equation.

Therefore, a SIDM model can produce both a cored profile and an isothermal profile. More detailed analysis shows that the density profile in the inner part of a core-collapsed halo (outside the secondary core) scales as $r^{-2.2}$. The slight deviation from r^{-2} is significant because the density slope is related to the velocity dispersion slope by

$$\frac{d \ln \nu}{d \ln r} = 1 + \frac{1}{2} \frac{d \ln \rho}{d \ln r}, \quad (3.41)$$

which can be derived from the hydrostatic equation (left as an exercise). Therefore,

$$\frac{d \ln \nu}{d \ln r} < 0 \quad \Rightarrow \quad \frac{d \ln \rho}{d \ln r} < -2. \quad (3.42)$$

A negative velocity dispersion slope is necessary for SIDM to evolve from a cored phase to a core collapsed phase. A negative velocity dispersion gradient means heat outflows from the core of the halo to its outskirts. Unlike typical thermal systems, an SIDM halo, viewed

as a gravothermal system, has a negative heat capacity. The heat outflow heats up the core, leading to more heat outflow, and the system's maximum entropy is infinite, resulting in a core-collapsed halo.

The evolution time from the initial NFW profile to the cored profile and then to the quasi-isothermal profile depends on the relaxation time of dark matter self-interaction. The relaxation time is given by

$$t_{\text{rlx}} = \frac{1}{n\sigma v} = \frac{1}{\rho(\sigma/m)v} = 1.5 \text{ Gyr} \left(\frac{0.4 \text{ GeV cm}^{-3}}{\rho} \right) \left(\frac{1 \text{ cm}^2 \text{ g}^{-1}}{\sigma/m} \right) \left(\frac{300 \text{ km s}^{-1}}{v_{\text{rel}}} \right). \quad (3.43)$$

Simulations show that it takes $t = \mathcal{O}(1) \times t_{\text{rlx}}$ for the halo to evolve from the initial NFW profile to the cored profile, and $t = \mathcal{O}(100) \times t_{\text{rlx}}$ for the halo to further evolve to the super-cuspy profile, corresponding to a core-collapsed halo. Note that this evolution time is strongly influenced by other factors, such as the halo concentration c_h , defined as the halo radius r_h over the scale radius r_s of the initial halo profile. In summary, SIDM halos can exhibit NFW, cored, or quasi-isothermal profiles depending on their evolution time and halo properties. This may allow SIDM to fully address the diversity problem.

There are many astrophysical probes of SIDM at different scales. We summarize the *allowed* values from these probes and the sweet spots for solving small-scale challenges in Fig. ?? as colored bars. From the plot, it is clear that a velocity-dependent cross-section strength is necessary for SIDM. This is effectively realized in the so-called Yukawa SIDM model. This model considers a light scalar with mass m_ϕ mediating the long-range force between dark matter particles with mass m_χ . The self-interaction is described by a Yukawa potential:

$$V(r) = \pm \alpha_\chi \frac{e^{-m_\phi r}}{r}, \quad (3.44)$$

where α_χ is the strength of the potential, m_ϕ is the mediator mass, and $+$ or $-$ represents a repulsive or attractive interaction, respectively. Given the differential scattering cross-section $d\sigma/d\Omega$ corresponding to $V(r)$, we compute the viscosity transfer cross-section as:

$$\sigma_V = \int \frac{d\sigma}{d\Omega} \sin^2 \theta d\Omega, \quad (3.45)$$

where θ is the scattering angle. The $\sin^2 \theta$ kernel appears from deriving the thermal conductivity [104], which should be the thermal quantity driving the gravothermal evolution of a SIDM halo. The parameter space of the model can be divided into three regimes: the perturbative Born regime ($\alpha_\chi m_\chi/m_\phi \ll 1$), the non-perturbative classical regime ($\alpha_\chi m_\chi/m_\phi \gg 1$, $m_\chi v/m_\phi \gg 1$), and the non-perturbative resonant regime ($\alpha_\chi m_\chi/m_\phi \gg 1$, $m_\chi v/m_\phi \ll 1$). This model exhibits a variety of velocity dependencies, as shown in Fig. 14, which is based on the parameters listed in Tab. 3.2. The computational details can be found in [105]. Note that Yukawa SIDM in small halos generally shows a large cross-section strength, which could push dwarf halos towards a core-collapsed phase.

	m_χ [GeV]	m_ϕ [MeV]	α_χ
Model 1	119	0.4	3.0×10^{-3}
Model 2	20	3.5	1.6×10^{-3}
Model 3	40	1.1	1.5×10^{-3}
Model 4	18	1.7	1.2×10^{-3}
Model 5	27	1.1	9.0×10^{-4}

Table 3. Benchmarks for the Yukawa SIDM model shown in Fig. 14.

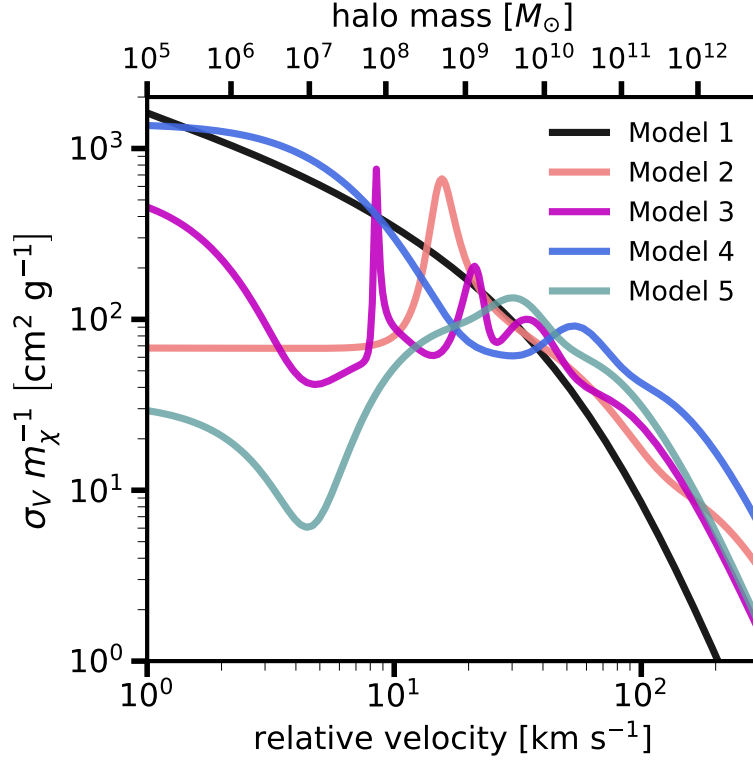


Figure 14. The viscosity transfer cross-section strength σ_V/m_χ for the five benchmark models listed in Tab. 3.2, plotted as a function of the relative velocity v (lower x-axis). The upper x-axis shows the halo mass with maximum circular velocity $v_{\text{max}} = v$. The plot is taken from [105].

Acknowledgments

Y.Z. would like to express gratitude to the organizers, Haipeng An, Lian-Tao Wang, Qing Wang, Yonglong Wang, and Zhong-Zhi Xianyu, for the opportunity to speak and for their efforts in organizing the event. It was a great pleasure to give these lectures, meet students from institutions worldwide, and visit Dai Gu, Linyi.

A Units

We often work with natural units, assuming $c = \hbar = k_B = \epsilon_0 = \mu_0 = 1$. In this setup, the elementary charge is $e = \sqrt{4\pi\alpha} = 0.303$. The basic unit conversions between natural units and SI units (kg, m, s, etc.) as well as astronomical units (M_\odot , pc, year, etc.) can be found at <https://github.com/ymzhong/naturalunit>.

B Cosmology for people in a hurry

B.1 Background

The evolution of the homogeneous contents of the universe follows the Friedman equation (assuming zero curvature) and the continuity equation. They are respectively given by

$$H^2 = \frac{8\pi G}{3}\rho = H_0^2 (\Omega_{r,0}a^{-4} + \Omega_{m,0}a^{-3} + \Omega_{\Lambda,0}), \quad \dot{\rho} = -3H(\rho + p). \quad (\text{B.1})$$

During different content-dominated eras, the universe expands differently. It evolves from an inflation era to a radiation era, then to a matter era, and finally to a dark energy era. Most of dark matter physics occurs during the radiation and matter eras. The dependence of the energy density ρ , the scale factor a , the Hubble parameter H , and the time t is summarized in Tab. 4.

Content	$w \equiv p/\rho$	ρ	a	H
Radiation	1/3	$\frac{3}{32\pi G t^2} \propto a^{-4}$	$\propto t^{1/2}$	$\frac{1}{2t} \propto a^{-2}$
Matter	0	$\frac{1}{6\pi G t^2} \propto a^{-3}$	$\propto t^{2/3}$	$\frac{2}{3t} \propto a^{-3/2}$
Vacuum	-1	$\frac{3H_0^2}{8\pi G} (\text{const.})$	$e^{H_0 t}$	H_0

Table 4. Different contents of the universe, their equations of state $w \equiv p/\rho$, and the relations between the energy density ρ , scale factor a , Hubble parameter $H \equiv \dot{a}/a$, and time t .

From the Planck measurement of Ω_m and COBE's measurement of the CMB temperature, one can find that matter-radiation equality occurs at $a_{\text{eq}} = 2.9 \times 10^{-4}$, which corresponds to $z_{\text{eq}} = 3400$ or $t_{\text{eq}} \sim 50,000$ years after the Big Bang. This is slightly before recombination at $z_{\text{rec}} = 1270$ or $t_{\text{rec}} \sim 300,000$ years after the Big Bang.

B.2 Thermodynamics in the early universe

Given a distribution function of a system of particles, $f(p, T)$, we can obtain its macroscopic quantities by taking the moment of the distribution function, i.e., integrating over the phase space with some kernel functions. The number density, energy density, and pressure for a given $f(p, T)$ are given by

$$n(T) = \frac{g}{(2\pi)^3} \int d^3p f(p, T), \quad (\text{B.2})$$

$$\rho(T) = \frac{g}{(2\pi)^3} \int d^3p f(p, T) E(p), \quad (\text{B.3})$$

$$P(T) = \frac{g}{(2\pi)^3} \int d^3p f(p, T) \frac{p^2}{3E(p)}. \quad (\text{B.4})$$

For bosons and fermions in the early universe, their number density, energy density, and pressure, under the relativistic limit, are respectively given by

$$n = \frac{\zeta(3)}{\pi^2} g T^3 \begin{cases} 1 & \text{boson} \\ \frac{3}{4} & \text{fermion} \end{cases}, \quad \rho = \frac{\pi^2}{30} g T^4 \begin{cases} 1 & \text{boson} \\ \frac{7}{8} & \text{fermion} \end{cases}, \quad P = \frac{\rho}{3} \quad (\text{B.5})$$

If they are non-relativistic, these quantities change to

$$n = g \left(\frac{mT}{2\pi} \right)^{3/2} e^{-m/T}, \quad \rho = mn + \frac{3}{2} nT, \quad P = nT, \quad (\text{B.6})$$

which are all Boltzmann suppressed ($\propto e^{-m/T}$). If there are multiple relativistic species, the energy density changes to

$$\rho = \frac{\pi^2}{30} g_*(T) T^4 \quad (\text{B.7})$$

where

$$g_* = \sum_{i=b} g_i \left(\frac{T_i}{T} \right)^4 + \frac{7}{8} \sum_{i=f} g_i \left(\frac{T_i}{T} \right)^4 \quad (\text{B.8})$$

The Standard Model at high temperature has 28 degrees of freedom for bosons and 90 degrees of freedom for fermions. Hence the corresponding $g_* = 106.75$.

From the first law of thermodynamics, we have $TdS = dU + PdV$. Now defining the entropy density $s \equiv S/V$ and substituting it together with $U = \rho V$ into the first law gives

$$(Ts - \rho - P)dV + V \left(\frac{Tds}{dT} - \frac{d\rho}{dT} \right) dT = 0 \quad (\text{B.9})$$

For the equation to be always valid, we need

$$s = \frac{\rho + P}{T}, \quad \frac{d(sa^3)}{dt} = 0, \quad (\text{B.10})$$

where the derivation of the second equation uses the continuity equation. For multiple relativistic species, from Eq. (B.7), we have

$$s = \frac{2\pi^2}{45} g_{*S}(T) T^3 \quad (\text{B.11})$$

where

$$g_{*S} = \sum_{i=b} g_i \left(\frac{T_i}{T} \right)^3 + \frac{7}{8} \sum_{i=f} g_i \left(\frac{T_i}{T} \right)^3 \quad (\text{B.12})$$

The entropy conservation, $d(sa^3)/dt$, implies

$$g_{*S}(T) T^3 a^3 = \text{const}, \quad \text{or} \quad T \propto g_{*S}^{-1/3} a^{-1}. \quad (\text{B.13})$$

It will be convenient to define $Y_i \equiv n_i/s$, which drops out a dependence if there is no particle creation or annihilation. For dark matter, if it is produced thermally, its abundance Y_i should not change since the freeze-out to today. Given $\rho_{\chi,0} = 10^{-11} \text{ eV}^4 = m_\chi n_{\chi,0}$ and $s_0 \simeq 10^{-11} \text{ eV}^3$, we have

$$Y_\chi \equiv \frac{n_\chi}{s} = \frac{\text{eV}}{m_\chi}. \quad (\text{B.14})$$

B.3 Dark matter thermal freeze-out

The dark matter thermal freeze-out happens when the Hubble parameter catches up with the annihilation rate of dark matter particles into the Standard Model particles.

$$n_\chi \langle \sigma v \rangle \sim H \sim \frac{T_{\text{fo}}^2}{m_{\text{pl}}}, \quad (\text{B.15})$$

where T_{fo} is the freeze-out temperature, which is around $m_\chi/10$. From this relation, one can estimate the dark matter abundance Y at freeze-out,

$$(Y_\chi)_{\text{fo}} = \frac{n_\chi}{s_{\text{fo}}} \sim \frac{T_{\text{fo}}^2}{m_{\text{pl}} \langle \sigma v \rangle T_{\text{fo}}^3} \sim \frac{\text{eV}}{m_\chi}. \quad (\text{B.16})$$

Given $T_{\text{fo}} \sim m_\chi/10$, we have

$$\langle \sigma v \rangle \sim \frac{10}{\text{eV} m_{\text{pl}}}. \quad (\text{B.17})$$

More careful computation shows the cross section needed to obtain the correct dark matter relic abundance is given by

$$\langle \sigma v \rangle = 3 \times 10^{-26} \text{ cm}^2/\text{s} = \frac{1}{(20 \text{ TeV})^2}. \quad (\text{B.18})$$

References

- [1] M. Cirelli, A. Strumia and J. Zupan, *Dark Matter*, [2406.01705](#).
- [2] S. Dodelson and F. Schmidt, *Modern Cosmology (2nd edition)*. Elsevier Science, 2020.
- [3] D. Baumann, *Cosmology*. Cambridge University Press, 2022.
- [4] T. Lin, *Dark matter models and direct detection*, *PoS* **333** (2019) 009, [[1904.07915](#)].
- [5] B. R. Safdi, *TASI Lectures on the Particle Physics and Astrophysics of Dark Matter*, *PoS TASI2022* (2024) 009, [[2303.02169](#)].
- [6] M. Schmaltz, “Lecture 1 on intro to dark matter.” <https://www.youtube.com/watch?v=WFLSxbcyHp8>, 2020.
- [7] F. Zwicky, *Die Rotverschiebung von extragalaktischen Nebeln*, *Helv. Phys. Acta* **6** (1933) 110–127.
- [8] P. Peebles, *Cosmology’s Century: An Inside History of Our Modern Understanding of the Universe*. Princeton University Press, 2020.
- [9] G. Bertone and D. Hooper, *History of dark matter*, *Rev. Mod. Phys.* **90** (2018) 045002, [[1605.04909](#)].
- [10] PLANCK collaboration, N. Aghanim et al., *Planck 2018 results. VI. Cosmological parameters*, *Astron. Astrophys.* **641** (2020) A6, [[1807.06209](#)].
- [11] N. Bellomo, K. V. Berghaus and K. K. Boddy, *Impact of freeze-in on dark matter isocurvature*, *JCAP* **11** (2023) 024, [[2210.15691](#)].
- [12] A. Strumia, *Dark Matter from freeze-in and its inhomogeneities*, *JHEP* **03** (2023) 042, [[2211.08359](#)].

- [13] D. Racco and A. Riotto, *Freeze-in dark matter perturbations are adiabatic*, *JCAP* **01** (2023) 020, [[2211.08719](#)].
- [14] I. Holst, W. Hu and L. Jenks, *Dark matter isocurvature from curvature*, *Phys. Rev. D* **109** (2024) 063507, [[2311.17164](#)].
- [15] A. Stebbins, *Generation of Isocurvature from Curvature Inhomogeneities on Super-Horizon Scales*, [2311.17379](#).
- [16] Y. Sofue, *Rotation Curve of the Milky Way and the Dark Matter Density*, *Galaxies* **8** (2020) 37, [[2004.11688](#)].
- [17] L. Hui, J. P. Ostriker, S. Tremaine and E. Witten, *Ultralight scalars as cosmological dark matter*, *Phys. Rev. D* **95** (2017) 043541, [[1610.08297](#)].
- [18] J. Alvey, N. Sabti, V. Tiki, D. Blas, K. Bondarenko, A. Boyarsky et al., *New constraints on the mass of fermionic dark matter from dwarf spheroidal galaxies*, *Mon. Not. Roy. Astron. Soc.* **501** (2021) 1188–1201, [[2010.03572](#)].
- [19] J. Lesgourgues and S. Pastor, *Neutrino mass from Cosmology*, *Adv. High Energy Phys.* **2012** (2012) 608515, [[1212.6154](#)].
- [20] M. Gerbino et al., *Synergy between cosmological and laboratory searches in neutrino physics*, *Phys. Dark Univ.* **42** (2023) 101333, [[2203.07377](#)].
- [21] DESI collaboration, A. G. Adame et al., *DESI 2024 VI: Cosmological Constraints from the Measurements of Baryon Acoustic Oscillations*, [2404.03002](#).
- [22] B. Allanach and H. E. Haber, *Supersymmetry, Part I (Theory)*, [2401.03827](#).
- [23] M. J. Strassler and K. M. Zurek, *Echoes of a hidden valley at hadron colliders*, *Phys. Lett. B* **651** (2007) 374–379, [[hep-ph/0604261](#)].
- [24] N. Arkani-Hamed, D. P. Finkbeiner, T. R. Slatyer and N. Weiner, *A Theory of Dark Matter*, *Phys. Rev. D* **79** (2009) 015014, [[0810.0713](#)].
- [25] PAMELA collaboration, O. Adriani et al., *An anomalous positron abundance in cosmic rays with energies 1.5–100 GeV*, *Nature* **458** (2009) 607–609, [[0810.4995](#)].
- [26] B. Fornal, *Neutron Dark Decay*, *Universe* **9** (2023) 449, [[2306.11349](#)].
- [27] Y.-S. Liu, D. McKeen and G. A. Miller, *Electrophobic Scalar Boson and Muonic Puzzles*, *Phys. Rev. Lett.* **117** (2016) 101801, [[1605.04612](#)].
- [28] J. L. Feng, B. Fornal, I. Galon, S. Gardner, J. Smolinsky, T. M. P. Tait et al., *Particle physics models for the 17 MeV anomaly in beryllium nuclear decays*, *Phys. Rev. D* **95** (2017) 035017, [[1608.03591](#)].
- [29] C.-Y. Chen, J. Kozaczuk and Y.-M. Zhong, *Exploring leptophilic dark matter with NA64- μ* , *JHEP* **10** (2018) 154, [[1807.03790](#)].
- [30] PLANCK collaboration, P. A. R. Ade et al., *Planck 2015 results. XIII. Cosmological parameters*, *Astron. Astrophys.* **594** (2016) A13, [[1502.01589](#)].
- [31] P. deNiverville, D. McKeen and A. Ritz, *Signatures of sub-GeV dark matter beams at neutrino experiments*, *Phys. Rev.* **D86** (2012) 035022, [[1205.3499](#)].
- [32] T. R. Slatyer, *Indirect dark matter signatures in the cosmic dark ages. I. Generalizing the bound on s-wave dark matter annihilation from Planck results*, *Phys. Rev.* **D93** (2016) 023527, [[1506.03811](#)].

- [33] M. J. Dolan, T. Ferber, C. Hearty, F. Kahlhoefer and K. Schmidt-Hoberg, *Revised constraints and Belle II sensitivity for visible and invisible axion-like particles*, *JHEP* **12** (2017) 094, [[1709.00009](#)].
- [34] Y. Kahn, G. Krnjaic, N. Tran and A. Whitbeck, *M^β : A New Muon Missing Momentum Experiment to Probe $(g-2)_\mu$ and Dark Matter at Fermilab*, [1804.03144](#).
- [35] A. Berlin, N. Blinov, G. Krnjaic, P. Schuster and N. Toro, *Dark Matter, Millicharges, Axion and Scalar Particles, Gauge Bosons, and Other New Physics with LDMX*, [1807.01730](#).
- [36] M. Battaglieri et al., *US Cosmic Visions: New Ideas in Dark Matter 2017: Community Report*, in *U.S. Cosmic Visions: New Ideas in Dark Matter*, 7, 2017, [1707.04591](#).
- [37] J. Liu, L.-T. Wang, X.-P. Wang and W. Xue, *Exposing the dark sector with future Z factories*, *Phys. Rev.* **D97** (2018) 095044, [[1712.07237](#)].
- [38] R. Bollig, H. T. Janka, A. Lohs, G. Martinez-Pinedo, C. J. Horowitz and T. Melson, *Muon Creation in Supernova Matter Facilitates Neutrino-driven Explosions*, *Phys. Rev. Lett.* **119** (2017) 242702, [[1706.04630](#)].
- [39] G. G. Raffelt, *Stars as laboratories for fundamental physics: The astrophysics of neutrinos, axions, and other weakly interacting particles*. 5, 1996.
- [40] E. Hardy and R. Lasenby, *Stellar cooling bounds on new light particles: plasma mixing effects*, *JHEP* **02** (2017) 033, [[1611.05852](#)].
- [41] S. Knapen, T. Lin and K. M. Zurek, *Light Dark Matter: Models and Constraints*, *Phys. Rev.* **D96** (2017) 115021, [[1709.07882](#)].
- [42] B. Batell, A. Freitas, A. Ismail and D. McKeen, *Flavor-specific scalar mediators*, [1712.10022](#).
- [43] J. H. Chang, R. Essig and S. D. McDermott, *Supernova 1987A Constraints on Sub-GeV Dark Sectors, Millicharged Particles, the QCD Axion, and an Axion-like Particle*, *JHEP* **09** (2018) 051, [[1803.00993](#)].
- [44] M. Pospelov and J. Pradler, *Big Bang Nucleosynthesis as a Probe of New Physics*, *Ann. Rev. Nucl. Part. Sci.* **60** (2010) 539–568, [[1011.1054](#)].
- [45] S. Navas and P. D. Group, *Review of particle physics*, *Phys. Rev. D* **110** (2024) 030001.
- [46] T.-H. Yeh, J. Shelton, K. A. Olive and B. D. Fields, *Probing physics beyond the standard model: limits from BBN and the CMB independently and combined*, *JCAP* **10** (2022) 046, [[2207.13133](#)].
- [47] B. D. Fields and K. A. Olive, *Implications of the non-observation of ${}^6\text{Li}$ in halo stars for the primordial ${}^7\text{Li}$ problem*, *JCAP* **10** (2022) 078, [[2204.03167](#)].
- [48] K. Akita and M. Yamaguchi, *A precision calculation of relic neutrino decoupling*, *JCAP* **08** (2020) 012, [[2005.07047](#)].
- [49] Z. Hou, R. Keisler, L. Knox, M. Millea and C. Reichardt, *How Massless Neutrinos Affect the Cosmic Microwave Background Damping Tail*, *Phys. Rev. D* **87** (2013) 083008, [[1104.2333](#)].
- [50] D. J. Fixsen, *The Temperature of the Cosmic Microwave Background*, *Astrophys. J.* **707** (2009) 916–920, [[0911.1955](#)].
- [51] K. M. Nollett and G. Steigman, *BBN And The CMB Constrain Light, Electromagnetically Coupled WIMPs*, *Phys. Rev. D* **89** (2014) 083508, [[1312.5725](#)].

- [52] C. Giovanetti, M. Lisanti, H. Liu and J. T. Ruderman, *Joint Cosmic Microwave Background and Big Bang Nucleosynthesis Constraints on Light Dark Sectors with Dark Radiation*, *Phys. Rev. Lett.* **129** (2022) 021302, [[2109.03246](#)].
- [53] P. F. Depta, M. Hufnagel and K. Schmidt-Hoberg, *ACROPOLIS: A generic fRamework fOr Photodisintegration Of LIght elementS*, *JCAP* **03** (2021) 061, [[2011.06518](#)].
- [54] A. Arbey, J. Auffinger, K. P. Hickerson and E. S. Jenssen, *AlterBBN v2: A public code for calculating Big-Bang nucleosynthesis constraints in alternative cosmologies*, *Comput. Phys. Commun.* **248** (2020) 106982, [[1806.11095](#)].
- [55] C. Pitrou, A. Coc, J.-P. Uzan and E. Vangioni, *Precision big bang nucleosynthesis with improved helium-4 predictions*, *Submitted to Phys. Rept.* (2018) , [[1801.08023](#)].
- [56] C. Pitrou, A. Coc, J.-P. Uzan and E. Vangioni, *A new tension in the cosmological model from primordial deuterium?*, *Mon. Not. Roy. Astron. Soc.* **502** (2021) 2474–2481, [[2011.11320](#)].
- [57] A.-K. Burns, T. M. P. Tait and M. Valli, *PRyMordial: the first three minutes, within and beyond the standard model*, *Eur. Phys. J. C* **84** (2024) 86, [[2307.07061](#)].
- [58] E. Nadler, *The faintest galaxies and their dark matter halos*, https://cosmology.lbl.gov/talks/Nadler_20.pdf, September, 2020.
- [59] N. Sabti, J. B. Muñoz and D. Blas, *New Roads to the Small-scale Universe: Measurements of the Clustering of Matter with the High-redshift UV Galaxy Luminosity Function*, *Astrophys. J. Lett.* **928** (2022) L20, [[2110.13161](#)].
- [60] S. Chabanier, M. Millea and N. Palanque-Delabrouille, *Matter power spectrum: from Ly α forest to CMB scales*, *Mon. Not. Roy. Astron. Soc.* **489** (2019) 2247–2253, [[1905.08103](#)].
- [61] K. Bechtol et al., *Snowmass2021 Cosmic Frontier White Paper: Dark Matter Physics from Halo Measurements*, in *Snowmass 2021*, 3, 2022, [[2203.07354](#)].
- [62] J. Lesgourgues, *Cosmological Perturbations*, in *Theoretical Advanced Study Institute in Elementary Particle Physics: Searching for New Physics at Small and Large Scales*, 2, 2013, [[1302.4640](#), DOI].
- [63] E. W. Kolb, *The Early Universe*, vol. 69. Taylor and Francis, 5, 2019, [[10.1201/9780429492860](#)].
- [64] P. Bode, J. P. Ostriker and N. Turok, *Halo formation in warm dark matter models*, *Astrophys. J.* **556** (2001) 93–107, [[astro-ph/0010389](#)].
- [65] A. Schneider, R. E. Smith, A. V. Maccio and B. Moore, *Nonlinear Evolution of Cosmological Structures in Warm Dark Matter Models*, *Mon. Not. Roy. Astron. Soc.* **424** (2012) 684, [[1112.0330](#)].
- [66] R. Feynman, R. Leighton and M. Sands, *The Feynman Lectures on Physics*. No. Vol. 1~3 in Addison-Wesley world student series. Addison-Wesley Publishing Company, 1963.
- [67] K. K. Rogers and H. V. Peiris, *Strong Bound on Canonical Ultralight Axion Dark Matter from the Lyman-Alpha Forest*, *Phys. Rev. Lett.* **126** (2021) 071302, [[2007.12705](#)].
- [68] M. A. Buen-Abad, R. Essig, D. McKeen and Y.-M. Zhong, *Cosmological constraints on dark matter interactions with ordinary matter*, *Phys. Rept.* **961** (2022) 1–35, [[2107.12377](#)].
- [69] E. O. Nadler, V. Gluscevic, K. K. Boddy and R. H. Wechsler, *Constraints on Dark Matter*

- Microphysics from the Milky Way Satellite Population*, *Astrophys. J. Lett.* **878** (2019) 32, [[1904.10000](#)].
- [70] DES collaboration, E. O. Nadler et al., *Milky Way Satellite Census. III. Constraints on Dark Matter Properties from Observations of Milky Way Satellite Galaxies*, *Phys. Rev. Lett.* **126** (2021) 091101, [[2008.00022](#)].
 - [71] O. Newton, M. Leo, M. Cautun, A. Jenkins, C. S. Frenk, M. R. Lovell et al., *Constraints on the properties of warm dark matter using the satellite galaxies of the Milky Way*, [2011.08865](#).
 - [72] N. Banik, J. Bovy, G. Bertone, D. Erkal and T. J. L. de Boer, *Novel constraints on the particle nature of dark matter from stellar streams*, [1911.02663](#).
 - [73] E. O. Nadler, S. Birrer, D. Gilman, R. H. Wechsler, X. Du, A. Benson et al., *Dark Matter Constraints from a Unified Analysis of Strong Gravitational Lenses and Milky Way Satellite Galaxies*, [2101.07810](#).
 - [74] W. Enzi et al., *Joint constraints on thermal relic dark matter from a selection of astrophysical probes*, [2010.13802](#).
 - [75] D. McCammon et al., *A High spectral resolution observation of the soft x-ray diffuse background with thermal detectors*, *Astrophys. J.* **576** (2002) 188–203, [[astro-ph/0205012](#)].
 - [76] A. L. Erickcek, P. J. Steinhardt, D. McCammon and P. C. McGuire, *Constraints on the Interactions between Dark Matter and Baryons from the X-ray Quantum Calorimetry Experiment*, *Phys. Rev. D* **76** (2007) 042007, [[0704.0794](#)].
 - [77] M. S. Mahdawi and G. R. Farrar, *Constraints on Dark Matter with a moderately large and velocity-dependent DM-nucleon cross-section*, *JCAP* **10** (2018) 007, [[1804.03073](#)].
 - [78] CRESST collaboration, A. H. Abdelhameed et al., *First results from the CRESST-III low-mass dark matter program*, *Phys. Rev. D* **100** (2019) 102002, [[1904.00498](#)].
 - [79] CRESST collaboration, A. H. Abdelhameed et al., *Description of CRESST-III Data*, [1905.07335](#).
 - [80] CRESST collaboration, G. Angloher et al., *Results on MeV-scale dark matter from a gram-scale cryogenic calorimeter operated above ground*, *Eur. Phys. J. C* **77** (2017) 637, [[1707.06749](#)].
 - [81] XENON collaboration, E. Aprile et al., *First Dark Matter Search Results from the XENON1T Experiment*, *Phys. Rev. Lett.* **119** (2017) 181301, [[1705.06655](#)].
 - [82] EDELWEISS collaboration, E. Armengaud et al., *Searching for low-mass dark matter particles with a massive Ge bolometer operated above-ground*, *Phys. Rev. D* **99** (2019) 082003, [[1901.03588](#)].
 - [83] W. Yin, *Highly-boosted dark matter and cutoff for cosmic-ray neutrinos through neutrino portal*, *EPJ Web Conf.* **208** (2019) 04003, [[1809.08610](#)].
 - [84] T. Bringmann and M. Pospelov, *Novel direct detection constraints on light dark matter*, *Phys. Rev. Lett.* **122** (2019) 171801, [[1810.10543](#)].
 - [85] C. Cappiello and J. F. Beacom, *Strong New Limits on Light Dark Matter from Neutrino Experiments*, *Phys. Rev. D* **100** (2019) 103011, [[1906.11283](#)].
 - [86] D. Wadekar and G. R. Farrar, *First astrophysical constraints on dark matter interactions with ordinary matter at low relative velocity*, [1903.12190](#).

- [87] T. Emken, R. Essig, C. Kouvaris and M. Sholapurkar, *Direct Detection of Strongly Interacting Sub-GeV Dark Matter via Electron Recoils*, *JCAP* **09** (2019) 070, [[1905.06348](#)].
- [88] R. Essig, A. Manalaysay, J. Mardon, P. Sorensen and T. Volansky, *First Direct Detection Limits on sub-GeV Dark Matter from XENON10*, *Phys. Rev. Lett.* **109** (2012) 021301, [[1206.2644](#)].
- [89] R. Essig, T. Volansky and T.-T. Yu, *New Constraints and Prospects for sub-GeV Dark Matter Scattering off Electrons in Xenon*, *Phys. Rev. D* **96** (2017) 043017, [[1703.00910](#)].
- [90] XENON10 collaboration, J. Angle et al., *A search for light dark matter in XENON10 data*, *Phys. Rev. Lett.* **107** (2011) 051301, [[1104.3088](#)].
- [91] XENON collaboration, E. Aprile et al., *Low-mass dark matter search using ionization signals in XENON100*, *Phys. Rev. D* **94** (2016) 092001, [[1605.06262](#)].
- [92] DARKSIDE collaboration, P. Agnes et al., *Constraints on Sub-GeV Dark-Matter–Electron Scattering from the DarkSide-50 Experiment*, *Phys. Rev. Lett.* **121** (2018) 111303, [[1802.06998](#)].
- [93] SUPERCDMS collaboration, R. Agnese et al., *First Dark Matter Constraints from a SuperCDMS Single-Charge Sensitive Detector*, *Phys. Rev. Lett.* **121** (2018) 051301, [[1804.10697](#)].
- [94] SENSEI collaboration, M. Crisler, R. Essig, J. Estrada, G. Fernandez, J. Tiffenberg, M. Sofo haro et al., *SENSEI: First Direct-Detection Constraints on sub-GeV Dark Matter from a Surface Run*, *Phys. Rev. Lett.* **121** (2018) 061803, [[1804.00088](#)].
- [95] SENSEI collaboration, O. Abramoff et al., *SENSEI: Direct-Detection Constraints on Sub-GeV Dark Matter from a Shallow Underground Run Using a Prototype Skipper-CCD*, *Phys. Rev. Lett.* **122** (2019) 161801, [[1901.10478](#)].
- [96] SENSEI collaboration, L. Barak et al., *SENSEI: Direct-Detection Results on sub-GeV Dark Matter from a New Skipper-CCD*, *Phys. Rev. Lett.* **125** (2020) 171802, [[2004.11378](#)].
- [97] Y. Ema, F. Sala and R. Sato, *Light Dark Matter at Neutrino Experiments*, *Phys. Rev. Lett.* **122** (2019) 181802, [[1811.00520](#)].
- [98] H. An, M. Pospelov, J. Pradler and A. Ritz, *Directly Detecting MeV-scale Dark Matter via Solar Reflection*, *Phys. Rev. Lett.* **120** (2018) 141801, [[1708.03642](#)].
- [99] T. Emken, *Solar reflection of light dark matter with heavy mediators*, [2102.12483](#).
- [100] D. J. Fixsen, E. S. Cheng, J. M. Gales, J. C. Mather, R. A. Shafer and E. L. Wright, *The Cosmic Microwave Background spectrum from the full COBE FIRAS data set*, *Astrophys. J.* **473** (1996) 576, [[astro-ph/9605054](#)].
- [101] Y. Ali-Haïmoud, J. Chluba and M. Kamionkowski, *Constraints on Dark Matter Interactions with Standard Model Particles from Cosmic Microwave Background Spectral Distortions*, *Phys. Rev. Lett.* **115** (2015) 071304, [[1506.04745](#)].
- [102] Y. Ali-Haïmoud, *Testing dark matter interactions with CMB spectral distortions*, *Phys. Rev. D* **103** (2021) 043541, [[2101.04070](#)].
- [103] S. Tulin and H.-B. Yu, *Dark Matter Self-interactions and Small Scale Structure*, *Phys. Rept.* **730** (2018) 1–57, [[1705.02358](#)].
- [104] E. M. Lifshitz and L. P. Pitaevskii, *Physical kinetics*. 1981.

- [105] D. Gilman, Y.-M. Zhong and J. Bovy, *Constraining resonant dark matter self-interactions with strong gravitational lenses*, *Phys. Rev. D* **107** (2023) 103008, [[2207.13111](#)].